The SACLA X-Ray Free-Electron Laser Based on Normal-Conducting C-Band Technology

Tsumoru Shintake

Contents

T. Shintake (✉)
Okinawa Institute of Science and Technology Graduate University (OIST), Onna-Son, Okinawa, Japan
e-mail: shintake@oist.jp

E. J. Jaeschke et al. (eds.), *Synchrotron Light Sources and Free-Electron Lasers*,
https://doi.org/10.1007/978-3-030-23201-6_9

Abstract

C-band (twice of S-band frequency) linear accelerator technology was initially developed for the future $e^+ e^-$ linear collider project. R&D took place from 1996 ∼ 2000, guided by the author at KEK (Group 1992; Shintake et al. 1995, 1998), followed by SCSS project (Shintake et al. 2001, 2003; Group 2004) at RIKEN/SPring-8 (2001 ∼ 2005), where we demonstrated high-gradient operation of a C-band accelerator. Based on the developed C-band technology, 400-m-long 8-GeV C-band accelerator was built at the SPring-8 site (2006 ∼ 2010) as the main linac to drive the X-ray FEL facility: XFEL/SPring-8, later renamed as "SACLA" (SCSS X-FEL R&D Group 2004; Shintake and XFEL/SPring-8 Joint Team 2010; Ishikawa et al. 2012). After 1,700 h of high-power conditioning, the maximum acceleration gradient reached 38 MV/m. The machine trip rate for each accelerator unit under nominal operation conditions is currently as low as once per day at a gradient of 35 MV/m and a repetition cycle of 30 pps. The measured stabilities of phase and amplitude of the rf field were 0.03° and 0.01% standard deviation, respectively. They were sufficient for the future upgrade to the seeded FEL operation. The first lasing was achieved in 2011, and since then, the C-band accelerator has been operated full-time, demonstrating fairly stable performance under continuous operation for 20,000 h. Twenty years of R&D was required from the first proposal to reach this point.

Introduction

An X-ray free-electron laser (X-ray FEL), which generates coherent and intense X-ray beams in a form of ultrashort pulse duration in femtosecond region, will boost research activities in various fields, such as material science, molecular biology, catalysis engineering, physiology, and medicine. The most promising scheme of the X-ray FEL is the self-amplified spontaneous-emission (SASE) scheme, which utilizes amplification phenomena on the monochromatic radiation from high-energy electron beam running through a periodic magnetic array called the undulator. Since this scheme does not require optical resonator cavity, SASE-based X-ray FEL can generate coherent radiation in the wide wavelength range from far infrared to hard X-rays.

The wavelength of X-ray FEL is defined by the characteristic wavelength of the undulator radiation, which is given by

$$\lambda = \frac{\lambda_u}{2\gamma^2}\left(1 + \frac{1}{2}K^2\right) \tag{1}$$

where λ_u is the period of the magnetic array and γ is the relativistic parameter of electron beam energy. K is the beam deflection parameter of the undulator field;

$$K = \gamma \cdot \theta \approx 0.1\, B_0(\mathrm{kG}) \times \lambda_u(\mathrm{cm}) \tag{2}$$

θ is the maximum deflection angle. For example, using an undulator having period 3 cm and $K = 2$, in order to obtain 1 Å radiation, we need $\gamma = 2 \times 10^4$, whose corresponding electron beam energy is as high as 10 GeV. This is the main reason why X-ray laser becomes a large-scale accelerator facility. Equation (1) represents Doppler effect of radiation field, i.e., by which the series of dipole radiations generated by the transverse acceleration on electron beam is compressed into X-ray wavelength; therefore, the electron beam has to be very close to the speed of the light, i.e., relativistic energy is required.

When a high-quality electron beam runs through the long undulator line, the undulator radiation overlaps with the running electron bunch itself, and the density modulation is created at X-ray wavelength through the interaction with radiated field. The density modulation generates high-power and coherent wave, which again adopts density modulation on the electron bunch further. This recursive process continues until it reaches to a saturation point, where radiation becomes fully transverse coherent and temporally coherent. This is the SASE FEL. The saturation power is tremendously higher than the ordinal undulator radiation (spontaneous radiation). For more detail, various papers can be found elsewhere.

To realize SASE FEL in X-ray (1 Å), we have to meet the following requirements:

1. High-energy electron beam: energy in $6 \sim 20$ GeV depending on the target wavelength and the undulator parameter. Energy stability requirement is roughly 0.1% r.m.s.
2. High-quality electron beam: typically the normalized emittance value is better than 1 μm r.m.s., and the peak current $1 \sim 3$ kA is required. To obtain such high-current beam, two or three stages of magnetic bunch compressors are used. At upstream of each chicane, energy chirp is applied on the electron bunch by accelerating the beam at off-crest of the rf field. Small fluctuation in rf phase results in a large fluctuation of peak current; therefore, rf phase error on upstream accelerators is very tight. To stabilize the peak current within 5–10% r.m.s., rf phase jitter has to be below 0.1° r.m.s. in the injector section.
3. Undulator line: typical length of 100 m, having a few cm magnetic period, and importantly the beam deflection parameter has to be high enough. $K = 2 \sim 4$ is required to realize high enough FEL gain at X-ray wavelength.
4. The electron orbit in the undulator has to be maintained in a straight line within transverse tolerance of a few μm width, which reflects tight tolerance on the undulator field and beam orbit control. The upstream accelerator has to provide fairly stable beam; position jitter of the incoming beam must be smaller than ~5 μm r.m.s.

In principle, any slow parameter drift can be corrected by feedback loops with proper beam monitoring system, while there is no practical method to correct fast pulse-to-pulse fluctuations. Therefore, the technical issue is how to eliminate the fast-moving error sources or random fluctuations from the system. There are two major fluctuating sources in X-ray FEL accelerator, a pulse laser for the

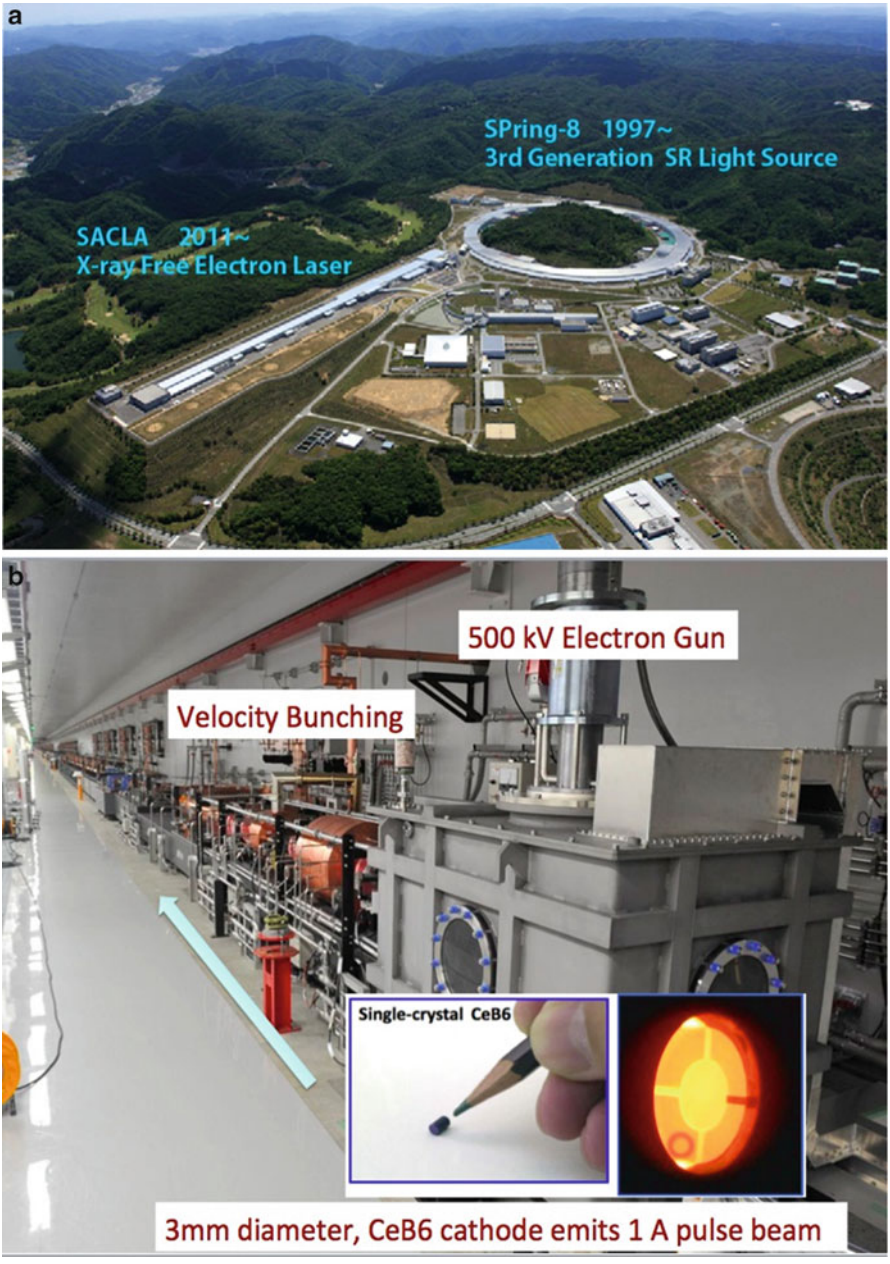

Fig. 1 (continued)

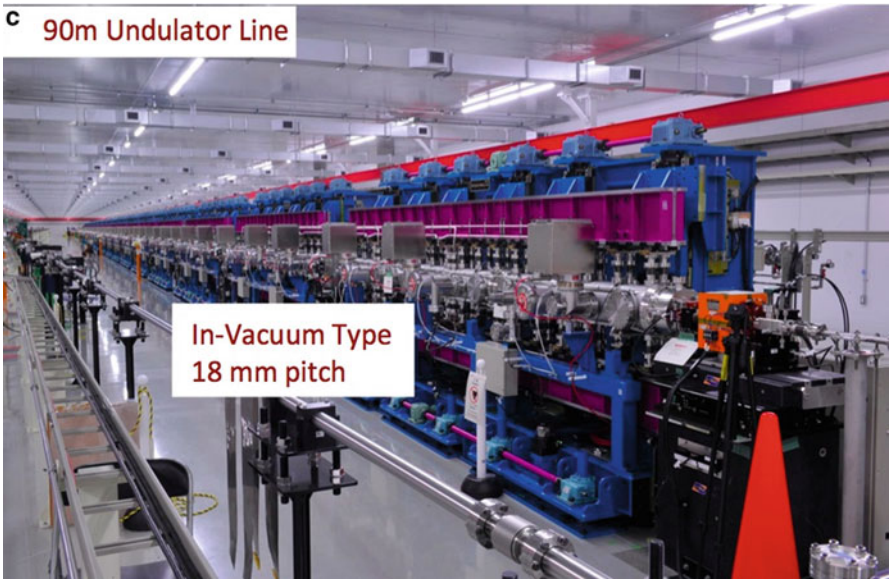

Fig. 1 SACLA X-ray FEL facility at SPring-8 Japan. (**a**) 700-m-long SACLA X-ray FEL facility was constructed at the SPring-8 site during 2006–2011. (**b**) A low-emittance electron beam is generated by the thermionic cathode, followed by velocity bunching and chicanes. (**c**) 90 long undulator line. 18 units of in-vacuum undulator are installed

photocathode electron gun and the thyratron tubes in the klystron modulators. If alternating technology is available, we should avoid using these technologies. If not, we have to focus on improving their performances.

Figure 1a shows SACLA X-ray FEL built right next to the synchrotron light source at SPring-8. The storage ring has been running for ten more years since 1997 as the third-generation light source. Figure 1b shows upstream end of the facility, where the thermionic electron gun is used to generate high-quality electron beam. In the main accelerator, 64 units of the C-band high-gradient accelerators have been installed as shown in Figs. 2 and 3, where the beam is accelerated up to 8 GeV within 400-m-long accelerator tunnel. Finally the beam is fed into 90-m-long undulator line to generate FEL radiation. Combination of the in-vacuum short-period undulator and the high -gradient C-band accelerator made possible to construct X-ray FEL in compact size fitting to available site length of 700 m. In contrast to this advantage, to make FEL in saturation in the short-period undulator having relatively lower K-parameter (nominal $\sim$1.8, maximum 2.2), a high-quality beam (low emittance) was required. To meet this request, we developed a thermionic electron gun using CeB_6 single crystal cathode, from which we extract the beam current of 1 A at 500 kV, followed by velocity bunching in subharmonic frequencies. Proof of principle experiment was performed at SCSS (SPring-8 Compact SASE Source) test accelerator, where generation of the high-quality beam was demonstrated; the slice emittance better than 0.7 μm at 250 A peak current was achieved after 250 times

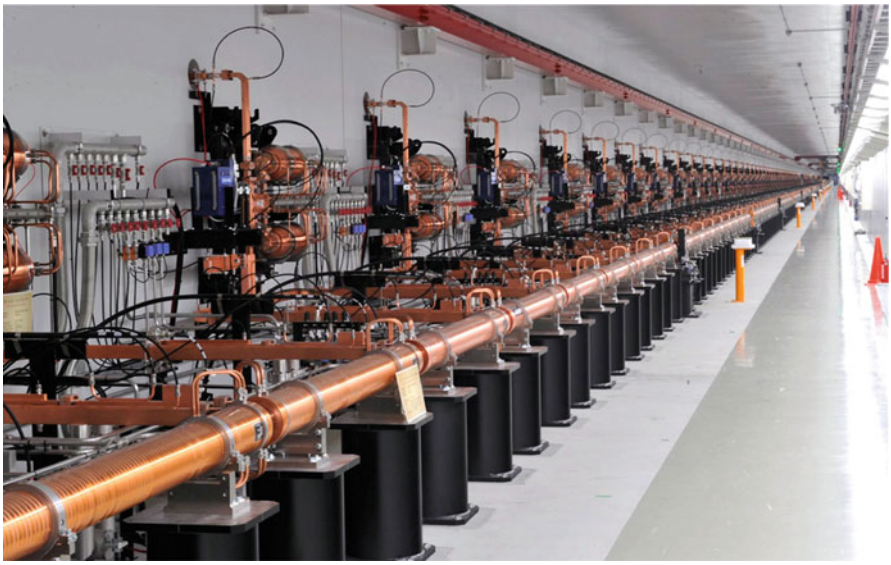

Fig. 2 C-band high-gradient accelerator in 400-m tunnel. A total of 128 accelerating structures have been installed to accelerate beams up to 8 GeV. Eight S-band accelerating structures are used in the injector part

Fig. 3 Klystron gallery houses 72 C-band klystrons modulators and associated controls, 8 S-band klystrons and modulators, and power supply for the electron injector

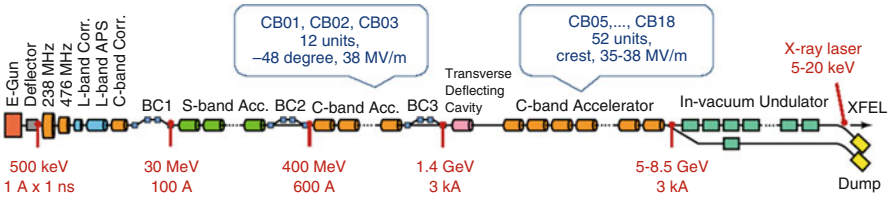

Fig. 4 Schematic configuration of the SACLA accelerator, where 64 units of the C-band system are used. Each unit consists of two accelerating structures, one klystron and its modulator power supply. Within active length of 230 m, the C-band accelerator can provide a maximum energy gain of 8.7 GeV. The injector complex uses subharmonic frequencies in order to perform velocity bunching

compression through velocity bunching and single-stage magnetic-chicane bunch compressor (Tanaka et al. 2006; Shintake et al. 2008, 2009). Later in SACLA project as shown in Fig. 4, the same electron source and compression scheme were employed, and two more magnetic chicanes were added to compress bunch ten times more. First lasing was achieved at 1 Å in June 2011, and after extensive beam tuning, the FEL power reached to 10 GW and pulse energy 0.3 mJ at 10 keV photon energy. The estimated slice emittance and beam current in the undulator section were 0.6 μm r.m.s. and 3 kA at 8.5 GeV, which were close to the theoretical emittance at the cathode, 0.4 μm r.m.s. at 1 A beam current. It means the slice emittance was kept almost unchanged through × 3,000 times bunch compression. This is a significant achievement in the beam physics of electron accelerators.

C-Band Choice

The author proposed C-band linear accelerator technology as the main linac in the future $e^+ e^-$ linear collider since 1992 (Group 1992; Shintake et al. 1995). I chose 5,712 MHz as the C-band frequency, which is exactly twice of 2,856 MHz, because this frequency has been widely used in the existing S-band electron accelerators, and the design of rf system becomes easier to synchronize frequencies if we chose C-band as the integer multiple of S-band. To synchronize with different S-band frequencies based on 2,998-MHz S-band klystrons in Europe, we need proper management of injection timing. In practice, it is possible to work with 5,712-MHz C-band and 2,998-MHz S-band ("SwissFEL Conceptual Design Report," PSI report 10-04, Paul Scherrer Institut, Villigen-PSI, Switzerland, 2010.).

C-band proposal was a personal conclusion after one-year sabbatical stay in the Frascati Laboratory in Rome (1990–1991), where I performed various thought experiments on machine designs for linear collider construction. I thought the first priority would be how to lower the construction cost, and at the same time to educe number of R&D items, while maintaining high reliability. The number of required components is fairly large, i.e., it requires a few thousand klystrons and modulators to construct 500-GeV center-of-mass energy linear collider based on

C-band accelerator technology; therefore, each component has to be very reliable and inexpensive.

First, I excluded the superconducting technology from my consideration because of its complexity and higher machine cost and also because there were less experiences on high-gradient acceleration using the superconducting RF cavity at that time. I thought it would require many years of R&D to establish reliable technology. Therefore, the linear collider itself would lose a chance to contribute to high-energy physics and would be out-competed by proton experiments using circular colliders.

From the point of view of accelerator structure efficiency, a higher frequency is desirable, since the shunt impedance scales with the driving frequency as (Neal 1966)

$$r \propto \omega^{1/2}, \tag{3}$$

where r is the shunt impedance per unit length. In steady-state conditions, the available accelerating gradient is

$$E_a = \sqrt{r\left(1 - e^{-2\tau}\right) P_{\text{in}}/L_1} \tag{4}$$

where τ is the attenuation constant, which is usually chosen close to 0.5. P_{in} is the input power to the accelerating structure, and L_1 is the structure length. For example, at X-band, the shunt impedance becomes twice as high as the S-band, which means we can get the same accelerating gradient with a half rf input power at the steady-state condition.

In the case of single-bunch or short-bunch operation, i.e., the pulse duration of rf input power is close to the rf filling time of the structure, we have to evaluate system performance with the integrated pulse energy in each pulse. The filling time of the structure is

$$t_F \propto \frac{2Q}{\omega}\tau \propto \omega^{-3/2}, \tag{5}$$

where Q is the quality factor of the resonant cavity cell. We see that the filling time becomes shorter at higher frequencies. Typically, it is 900 ns at S-band, 300 ns at C-band, and 100 ns at X-band. Assuming a pulse length compression ratio of 5 in the rf-pulse compressor, and including the beam pulse length, the pulse length at the klystron output becomes 7 μs at S-band, 2.5 μs at C-band, and 800 ns at X-band. From the point of view of pulse power supply technology for klystrons, 3∼10 μs (C- or S-band) is suitable for the conventional line-type modulator using PFN (pulse-forming network) with reasonable power efficiency. This type of power supply has been widely used in electron linear accelerators and whose technology has been well established.

From Eqs. (4) and (5), we have rf pulse energy fed into the structure as follows.

$$W_{\mathrm{RF}} = P_{\mathrm{in}} \cdot t_F = \frac{\tau}{\left(1 - e^{-2\tau}\right)} \frac{2E_a^2 L_1}{\omega r/Q} \propto \omega^{-2} E_a^2 L_1 \tag{6}$$

We have to note that the impedance parameter in this equation is r/Q, not r. r/Q represents geometric efficiency, which scales as $r/Q \propto \omega$. At C-band, r/Q is twice higher than S-band, and therefore the energy efficiency becomes much higher in C-band.

In order to cure multi-bunch instability, we employ the choke-mode structure in our C-band system. It possesses more volume than the simple disk-loaded structure, and thus it stores more energy, as the results r/Q drops by 10%. This is the price we need to pay more electricity consumption for the benefit of multi-bunch capability. In the entire accelerator facility, fraction of this loss becomes negligibly small, since we spent extra power on magnets, cooling water pumps, air conditioners, and chillier.

Figure 5 shows cross-sectional area of the rf structure at different frequencies. The stored energy is simply proportional to its volume, i.e., a product of length and cross-sectional area, which scales as $V \propto D^2 L \propto \omega^{-2}$, and it becomes quickly smaller at higher frequency.

We see that rf-pulse energy filled into the structure per unit length scales as $W_{\mathrm{RF}}/L \propto \omega^{-2} E_a^2$, and at higher frequency, rf-pulse energy required to fill the structure becomes quickly smaller. This is the main reason for choosing a higher frequency than the traditional S-band frequency. If we use C-band, we can obtain twice as high an accelerating gradient with the same rf-pulse energy filling the accelerating structure per unit length.

In practical design, we have to note that optimum length of the accelerating structure scales as $L = v_g t_F \propto \omega^{-1.5}$. Typically, it is 3 m long at S-band. If we keep the same group velocity, the optimum structure length at C-band becomes 1 m. This is too short, since we have to fabricate as many as three times the number of accelerating structures as for S-band. Each accelerating structure also needs input and output couplers; thus production cost becomes much higher. In our design we made the structure length $L = 1.8$ m. If we try to make structure length further longer, the group velocity becomes higher, which requires a larger iris aperture; thus, the shunt impedance r/Q drops, unfortunately. By compromising those parameters,

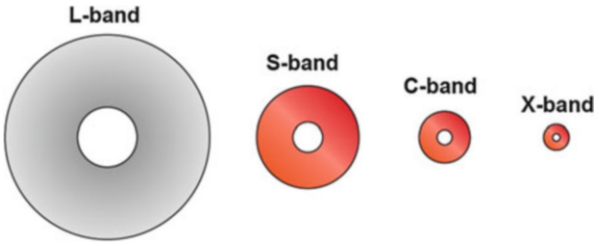

Fig. 5 Frequency scaling of the accelerating structure. Diameter and cross-sectional area scale as $D \propto \lambda \propto \omega^{-1}$, $S \propto \omega^{-2}$, respectively. At L-band, the superconducting technology is commonly chosen

we found the optimum length around 1.8 $\sim$ 2.2 m. We chose 1.8 m to make fabrication processes easy.

A higher frequency band, such as X-band, is desirable for lowering the required rf-pulse energy, while engineering of high-power rf sources becomes rather difficult. The high-power klystron at higher frequency band has technical risks. It requires the driving beam to be focused into a smaller diameter; thus, the beam becomes extremely high density, resulting in higher risk of damage on the interior structure of the klystron itself. In order to avoid collisions of the beam to the drift-tube wall, the size of the cathode in the electron gun must be made smaller; thus the beam diameter diminishes. It reflects to lowering current and rising the gun voltage to maintain the same beam power (the beam perveance value becomes smaller). It causes a higher risk of high-voltage breakdown in the electron gun and the output cavity. If the beam focusing is wrongly designed or fabrication of the focusing magnet is flawed, part of the beam will collide with the drift-tube wall and evaporate copper, which will trigger high-voltage breakdowns in the gun region and the output cavity. In a worst case, meltdown of the copper drift tube would occur. These symptoms limit the maximum power available from the practical klystron tubes. Roughly speaking, the output rf-pulse energy from the pulse klystron scales as

$$P \cdot t \propto \omega^{-2} \tag{7}$$

Toshiba E-3712 tubes can produce 80 MW $\times$ 4 μs = 320 J/pulse at S-band, which scales to 80 J/pulse at C-band. I chose the C-band klystron parameter as 50 MW $\times$ 2.5μs = 125 J/pulse, which is still 50% higher than expected from Eq. (7). To keep a safety margin, we employed a three-cell traveling output structure, which reduces 30% rf voltage across the output gap. Assuming power conversion efficiency of 45%, we chose the driving beam parameter as 350 kV $\times$ 320 A and 5 μs pulse width. This is technically an achievable parameter, i.e., the electron gun voltage lower than 400 kV will not cause HV breakdown problem around the anode gap and insulating ceramic. The beam current of 320 A is available from the cathode of 70-mm diameter with emission density as low as 6.3 A/cm^2, which is a suitable value to the dispenser-type cathode.

At even higher frequency bands, together with the higher voltage request on the driving beam and a shorter pulse length due to the short filling time, the klystron power supply becomes one of the most troublesome devices. At C-band, we could still use a conventional power supply technology, where the required voltage and pulse width are moderate, and thus a highly reliable system has been established.

There are additional technical problems in the higher frequency accelerators; the dimensional tolerance of the accelerating structure associated with the higher wakefield impedance becomes tight, which makes the fabrication cost higher and the production time longer. The alignment tolerance of the structure in the transverse direction scales as

$$\Delta y \propto \left(\frac{dW_T}{ds} \right)^{-1} \propto a^4 \propto \omega^{-4} \tag{8}$$

where a is the beam hole radius and W_T is the single-bunch wake function. We see that the alignment tolerance becomes very tight at higher frequency. At the C-band, alignment tolerance is 30 μm for a 1.6 nC charge in the linear collider, which will be achieved by means of proper beam monitoring devices and beam-based alignment scheme. In the case of X-ray FEL, the bunch charge is much lower and the accelerator length is much shorter, and as a result, the alignment tolerance on the accelerating structures becomes much looser. In our design it is in mm range, where the traditional alignment scheme is enough to meet this requirement.

By taking into account all these effects, I concluded that the C-band would be the best choice for the linear collider and also X-ray FELs. I assumed 35 MV/m as the nominal accelerating gradient, which is roughly twice the gradient in conventional S-band accelerators (Shintake et al. 1997a).

C-Band System Design

Here we consider proper system configuration under certain boundary conditions, such as, the same target final energy G_F(eV). The number of the accelerating structure required to reach G_F is

$$N_{\mathrm{acc}} = \frac{G_F}{E_a L_1} \tag{9}$$

where E_a is the accelerating gradient and L_1 is the unit length of the accelerating structure. If we run the machine at repetition rate f_{rep}(Hz), the wall plug AC power to generate rf power for the entire accelerator becomes

$$\begin{aligned} P_{\mathrm{AC}} &= \frac{1}{\eta_{\mathrm{sys}}} f_{\mathrm{rep}} \cdot N_{\mathrm{acc}} \times W_{\mathrm{RF}} \\ &= \frac{f_{\mathrm{rep}} G_F}{\eta_{\mathrm{sys}}} \cdot \frac{2\tau E_a}{\left(1 - e^{2\tau}\omega r/Q\right)} \\ &\propto \omega^{-2} \end{aligned} \tag{10}$$

where η_{sys} is the power conversion efficiency from wall plug AC power to rf power, which consists of

$$\eta_{\mathrm{sys}} = \eta_{\text{AC-HV}} \times \eta_{\text{HV-pulse}} \times \eta_{\mathrm{Klystron}} \times \eta_{\mathrm{WG}} \tag{11}$$

where the factors and typical values (almost the same for S- and C-bands) are:

$\eta_{\text{AC-HV}}$: Wall plug AC power to HV pulse, typically $0.7 \sim 0.8$.
$\eta_{\text{HV-pulse}}$: Useful part of HV pulse, rise and fall parts become power losses; $0.6 \sim 0.8$.
η_{Klystron}: Klystron power conversion efficiency; ~0.4.

η_{WG}: Power transfer efficiency from the klystron to the acceleration input, including RF-pulse compressor; $0.5 \sim 0.6$.

Taking into account all factors, the total system power conversion efficiency becomes roughly

$$\eta_{\mathrm{sys}} \approx 0.1. \tag{12}$$

In case of the superconducting L-band accelerator of ILC-type design (in pulse mode operation), this number becomes higher, while we have to take into account the electricity power consumption for LiHe-cooling system.

Here we start to design a C-band accelerator system. We firstly scale down all dimensions from existing S-band by factor $\times 1/2$ as shown in Fig. 6, which becomes an ideal C-band system. Maxwell's equation consists of a set of first-order time-space differential equations on the field components, and therefore, a simple scaling should work. It means that we have the identical eigenmode, i.e., having the same field profile, while its resonance frequency becomes twice higher. However, the skin depth of rf current flowing on copper wall becomes thinner by $1/\sqrt{2}$ times according to the relation $\delta \propto \omega^{-0.5}$; thus, the input rf wave

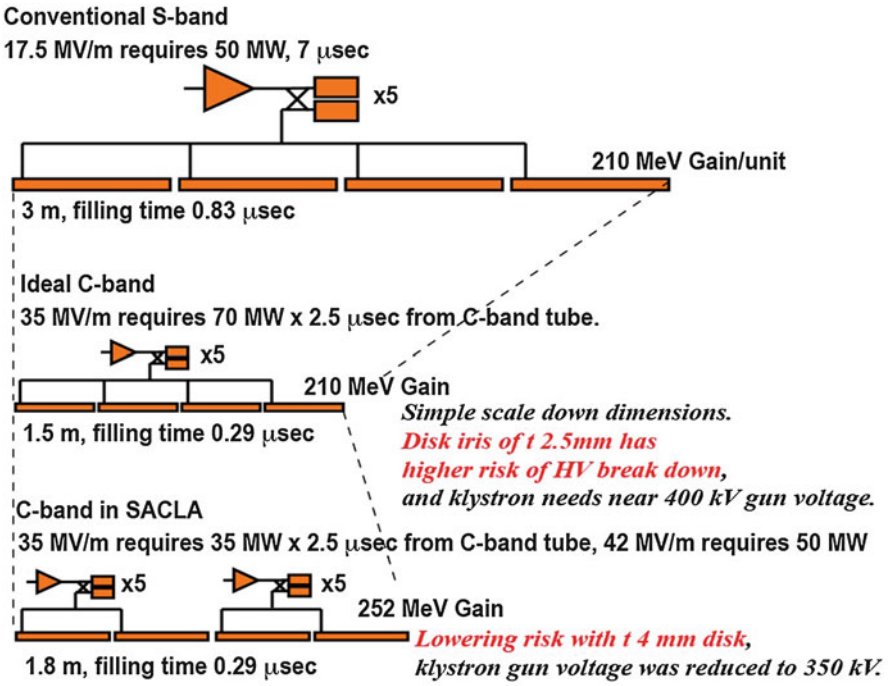

Fig. 6 Scaling from S-band to C-band system. (*Top*) conventional S-band, (*middle*) ideal C-band using simple scale-down dimensions from S-band, and (*bottom*) the practical C-band system currently used in SACLA

decays faster along with the accelerating structure, and as a result, the accelerating gradient at downstream becomes much lower. To compensate this effect, we have to make the iris size slightly larger and the group velocity $\sqrt{2}$ times faster; as a result, the attenuation constant τ comes back to the original value around 0.5 (for optimum power efficiency). This correction makes the shunt impedance slightly lower (8∼10%).

In Table 1, we see that we can achieve twice higher accelerating gradient using C-band; thus, the total accelerator length becomes half to reach the same target beam energy, while the AC power consumption is still half in case of ideal C-band. To upgrade accelerator from S-band to C-band using the same accelerator tunnel and if we remain the same accelerating gradient, we will be able to multiply repetition frequency four times, i.e., 240 pps, with the same amount of AC power consumption. We have to note that in a realistic accelerator, we also need electricity for various components: focusing magnets and heater for klystron and magnets for high-energy electron optics and infrastructures (cooling water, air conditioner, room illumination, and computers), total electricity consumption becomes much higher.

There are several technical difficulties to realize the ideal C-band system. The klystron of 70 MW peak output power requires higher voltage on the electron gun close to 400 kV, which will cause higher risk of high-voltage breakdown around the gun part and also output cavity. To make reliability higher, we limited the output power to be 50 MW and designed single klystron to drive two accelerating

Table 1 Parameter of S-band and C-band accelerators

	S-band	Ideal C-band	C-band in SACLA
Frequency (MHz)	2,856	5,712	5,712
Final energy (GeV)	8	8	8
Accelerating gradient (MV/m)	17.5	35	35
Active length (m)	457	229	229
Cavity type and mode	Disk-load	Disk-load	Choke-mode
Phase advance and taper	$2\pi/3$ CG	$2\pi/3$ CG	$3\pi/4$ CG
Disk thickness (mm)	5	2.5	4
Shunt-impedance r (average MΩ/m)	56	78	55
Q-factor	13,300	9,400	10,000
Shunt-impedance r/Q (average kΩ/m)	4.2	8.4	5.5
Attenuation constant τ	0.57	0.57	0.53
Filling time t_{F} (ns)	840	300	296
Structure length (m)	3	1.5	1.8
Input power to structure (MW)	24	35	62
Pulse length to structure (μs)	1.4	0.5	0.5
Klystron pulse length (μs)	7	2.5	2.5
Machine repetition f_{rep}(Hz)	60	60	60
AC Power at 60 Hz (MW)	3.2	1.6	2.3

structures. The klystron requires moderate gun voltage: 350 kV. Another problem is the higher surface electric field on the disk irises in the accelerating structure associated with field concentration to thinner disk edge. To lower the risk of the high-voltage breakdown, we made iris thickness from 2.5 to 4 mm, and with this change the field intensity was reduced more than 30% from original value, while the rf to beam coupling becomes lower, i.e., r/Q is lowered roughly 10%. In SACLA, we use the choke-mode cavity for damping HOM in the case of multi-bunch operation, in which r/Q is lowered 10% due to larger stored energy inside the choke structure. Finally, practical r/Q value becomes 5.5 kΩ/m. The figure of merit of C-band can be estimated by comparing Eq. (10), i.e.,

$$\frac{(\omega r/Q)_C}{(\omega r/Q)_S} = \frac{5{,}712\,\mathrm{MHz} \times 5.5\,\mathrm{k\Omega/m}}{2{,}856\,\mathrm{MHz} \times 4.2\,\mathrm{k\Omega/m}} \approx 2.6 \tag{13}$$

There is more than factor 2 improvement of power efficiency, so we can raise the accelerating gradient by factor 2 or more with the same amount of power usage as shown in Eq. (10).

The third model in the bottom of Fig. 6 shows the practical C-band system designed by taking into account all modifications mentioned above, which we currently use in the main accelerator at SACLA. To reduce the number of accelerator unit, the accelerating structure length was made 20% longer from 1.5 to 1.8 m. One C-band klystron feeds two accelerating structures and generates accelerating gradient 35 MV/m with 35-MW klystron output and in maximum 42 MV/m with 50 MW full powers.

Configuration of C-Band Acceleration Unit in SACLA

Figures 7 and 8 show the configuration of the C-band acceleration unit. In order to obtain high acceleration gradient, 50 MW pulse klystrons (Ohkubo et al. 1998) are used to supply high rf power to two traveling-wave acceleration structures, through SLED-type rf-pulse compressor. At nominal operation, the klystron output power of 40 MW can generate 38 MV/m. Output power of 40 MW is 80% of 50 MW maximum available power, and there is enough safety margin for assuring long-term reliability. In the pulse compressor, the rf-pulse width is compressed from 2.5 to 0.5 μs, to multiply the rf power by roughly four times. In case of multi-bunch operation, we need to generate flat pulse shape (200 ns flat top) in compressed power, and the power compression ratio becomes as low as 3. The rf power is fed into two quasi-constant-gradient-type acceleration structures, which are 1.8 m long each, generating an acceleration gradient of up to 38 MV/m for a single bunch. Thus, the beam energy gain of a 4-m-long C-band acceleration unit is about 136 MeV. The machine repeats pulse operation at 60 Hz in maximum. Figure 9 shows detail machine cycle.

The power loss in the waveguide from the klystron to the acceleration structure is about 10%, including the Ohmic losses on the inner surface of the copper waveguide

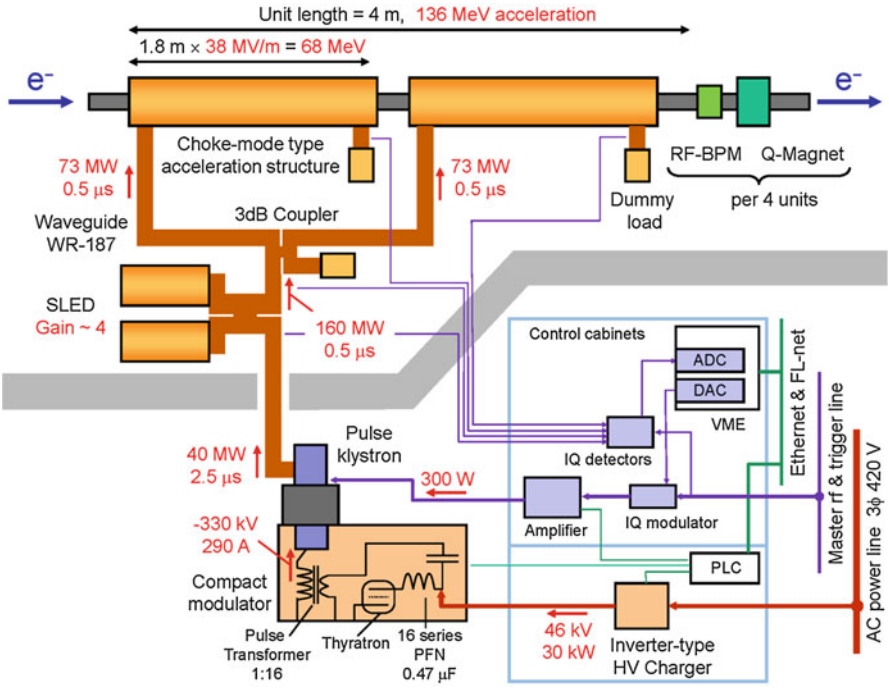

Fig. 7 Configuration of the C-band acceleration unit. Typical parameters for nominal operation are given in the figure

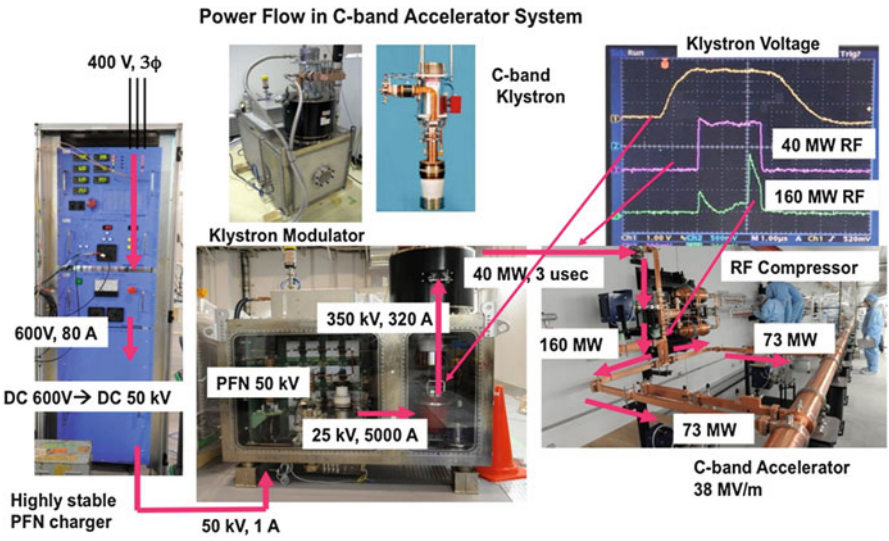

Fig. 8 Power flow in one unit of C-band accelerator

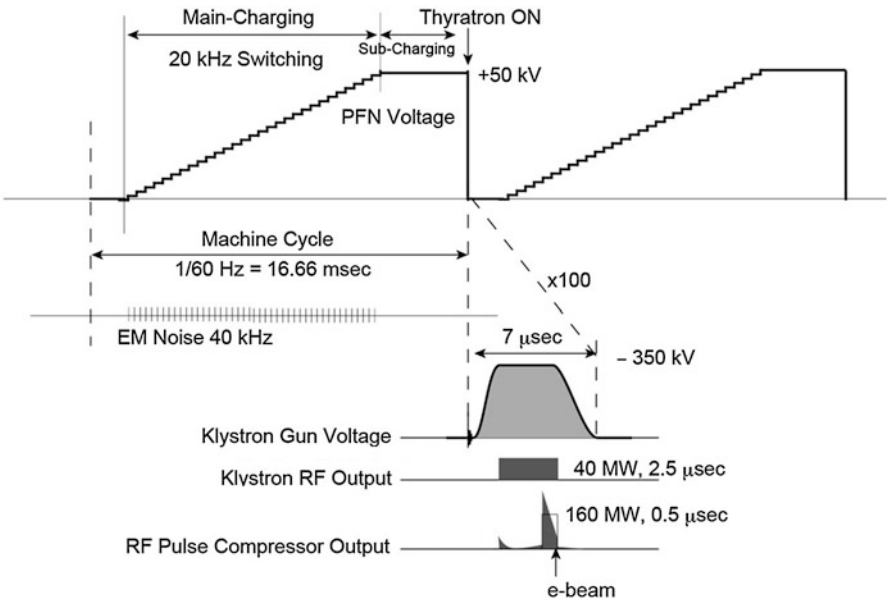

Fig. 9 Power supply machine cycle. Within 16.7-ms period, the machine repeats operation cycle as shown in this diagram; charging PFN capacitor, turn on thyratron, generating 350-kV pulse, 40 MW rf power generation from klystron, rf-pulse compression into 0.5 μs pulse, filling rf power into accelerating structure, and e-beam acceleration

and reflections at the waveguide flanges. At the end of the acceleration structure, the residual rf power is damped by a dummy load, in which silicon-carbide (SiC) disks are used as microwave absorbers. The rf powers are monitored at various locations: the klystron output, the rf-pulse compressor output, and the acceleration structure exit via rf directional couplers placed along the waveguides.

In order to prevent the vacuum components from high-voltage breakdown due to high rf electric field, the vacuum pressure is kept less than 10^{-6} Pa by means of five sputter-ion pumps attached to the waveguides. In case of a klystron failure, to replace the klystron without venting the vacuum in the acceleratory system, the rf window is commonly prepared to isolate klystron and waveguide vacuum. However, this rf window introduces additional source of hardware troubles, such as rf breakdown and ceramic puncture, and also makes vacuum system more complex, i.e., we need to add additional vacuum pumping system to pump locally closed volume between the rf window in the waveguide and the klystron rf window. On the other hand, in recent years the klystron technology has advanced dramatically, and the lifetime of the high-power pulse klystrons usually exceed a few 10,000 h. Since mean-time failure is so long, if we replace some klystrons in scheduled machine shutdown time, for example, replace klystron having a symptom of increasing HV trip rate, we may keep running the machine nicely. With this circumstance, we decided to eliminate the rf window from the waveguide system.

We prepared the gate valves in each two accelerator units in the tunnel to limit the number of the accelerating structures to be purged to atmospheric pressure for the klystron replacement and reduce required time for high-power processing after the maintenance.

In order to install klystrons and modulators in narrow 4-m spaces, we developed a compact oil-filled klystron modulator combined with an inverter-type high-voltage charger. Their size has been drastically reduced as compared to the conventional open-air-type modulators. The klystrons, modulators, and control enclosures are arrayed in series along the klystron gallery as already shown in Fig. 3. The traditional line-type pulse-forming network (PFN) circuit with a thyratron tube as a high-voltage switch has been employed. Variation of the charging voltage on PFN capacitor is one of the largest sources of the rf phase and amplitude fluctuation. To meet requirements of rf stability of 0.01% in amplitude, the voltage regulation of our high-voltage charger was substantially improved by introducing specially designed circuitry.

Intensive efforts have been made on LLRF system to meet the stability requirement. The driving rf input power to the klystron is individually supplied by a 500-W solid-state amplifier, which is capable of saturating the klystron so as to make the output power insensitive to various fluctuations, such as driving rf power change or gain fluctuation due to drive beam parameter variations. The amplitude and phase modulations are applied on the input rf signal by means of in-phase and quadrature (IQ) modulator circuit, which is integrated as a part of the LLRF system (Maesaka et al. 2008). To monitor the rf signals from rf pickups, the LLRF system also provides rf vector detectors, using IQ detectors connected to 12-bit or 16-bit ADC converter. The measured rf phase is compared to the preset target values, and computed feedback signal is generated through IQ modulator controlled by a VERSA-module Europa bus (VME) computer. In order to avoid phase drift due to ambient temperature changes, the LLRF system and the solid-state amplifier were housed inside the temperature-regulated 19-in. cabinet as shown in Fig. 10. The forced airflow circulates in a closed loop through a heat exchanger, which is cooled by the temperature-regulated water connected to the accelerator utility system. Beam position monitor electronics is also implemented in this system (Otake et al. 2013).

The temperature stability of the cooling water in the utility system is around $\pm 0.2\,^{\circ}\mathrm{C}$. This cooling water is supplied to the klystron, modulator, control cabinet, and the solid-state amplifier. Much higher stability is required on the accelerating structure and the rf-pulse compressor, since phase and resonance frequency are very sensitive to the mechanical dimensions; thus, a special temperature feedback system has been developed. Using an electric heater immersed in flowing water at inlet to these devices and monitoring temperature on the devices, the control power provides to the heater and stabilizes the temperature within $\pm 0.02\,^{\circ}\mathrm{C}$, which corresponds to an rf phase stability of $\pm 0.2^{\circ}$ for the acceleration structure and $\pm 0.3^{\circ}$ for the pulse compressor output.

All of these components are controlled by a PLC-based feedback system and VME modules housed in the control cabinet. They are remotely controlled and

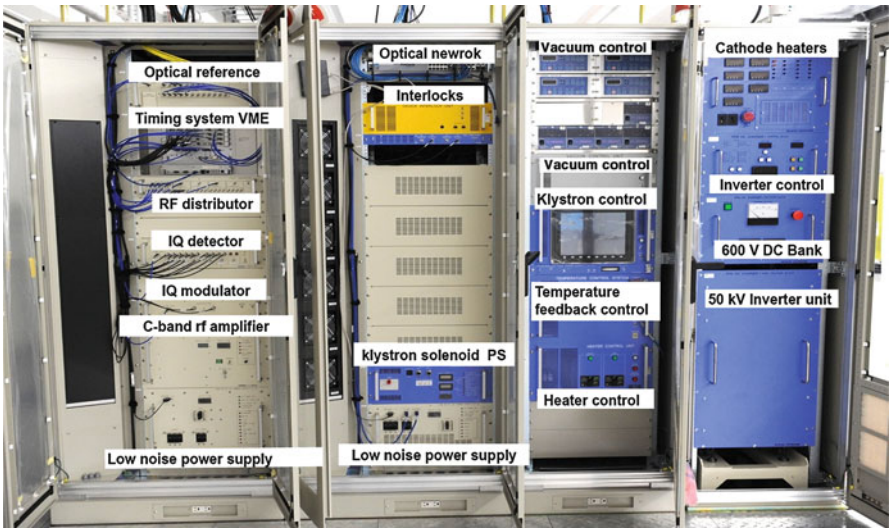

Fig. 10 LLRF system and klystron modulator controls

monitored at the control room via the MADOCA framework (Tanaka et al. 2011). Manual operation from operators or automatic control sequences sets various parameters in each unit, such as the charging voltage, the rf phase, the pulse timing, and the repetition rate. This control system allows us to operate the accelerator system in flexible manner. In order to recover quickly from various machine troubles, several "standby" units are preserved and run at off-beam timing at 10 μs before the beam-arrival timing; thus, it does not contribute to the beam acceleration. If a certain problem occurs in one of the "in-service" units, the operator switches the standby unit to in-service units so as to recover the acceleration energy gain.

C-Band Waveguide Component

C-Band Waveguide and Flange

When we started C-band R&D in 1996, there were no available C-band waveguide components capable of handling tens of megawatt level of rf power with vacuum tight design. Therefore we needed to develop every waveguide components, even the copper waveguide itself (Matsumoto et al. 1997). At C-band frequency 5,712 MHz, there are two choices for the waveguide size: one is EIA-WR187 (3.93–5.85 GHz), and the other is EIA-WR159 (4.9–7.05 GHz). We chose EIA-WR187, which has an inner cross section of 47.55 mm wide and 22.15 mm high, because of its lower transmission loss close to existing S-band waveguide. The theoretical transmission loss of EIA-WR187 waveguide is −0.032 dB/m at 5,712 MHz, which is comparable to the attenuation −0.021 dB/m at S-band in EIA-WR284 (at 3 GHz,

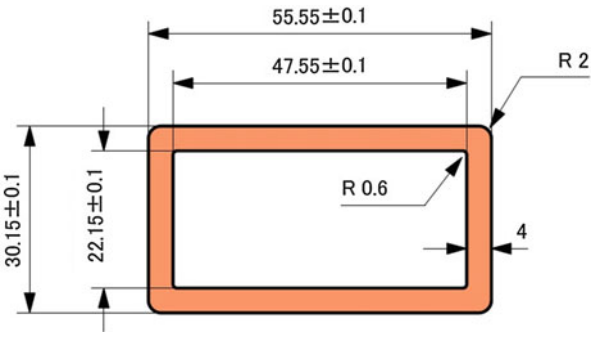

Fig. 11 C-band waveguide cross section. Inner dimension is based on EIA-WR187

72.1 × 34.0 mm). Figure 11 shows the waveguide cross section. The thickness of the copper wall was determined 4 mm, so as to make the fabrication process easier, especially brazing for metal-to-metal bonding. Accuracy of the inner dimension is $< \pm 0.1$ mm, which corresponds to phase error of 3.6°/m; thus, we need careful control of electrical length during fabrication process.

One practical problem in this choice is that if we chose C-band frequency at the second harmonic frequency of the European S-band frequency, i.e., 5,997.0 MHz = 2 × 2,998.5 MHz, which is too close to the cutoff frequency of the higher-order mode (TE_{20}) in EIA-WR187 at 6.3 Hz. There is a risk of mode mixing between TE_{20} and TE_{10} at any irregular structure inside the waveguide, such as the flange connection or the monitor port, which will cause excess power loss and local heat, or multipacting discharge. Therefore, it is desirable to use 5,712-MHz C-band.

The high-power performance of the waveguide system is sometimes limited by outgassing problem from the inner surface of the copper waveguide. The copper waveguide is made by several steps of extrusion processes from a bare copper block, where the lubricating greases are normally used to reduce friction and make the copper surface smoother. Unfortunately some of these lubricants are buried into copper body and cause contaminations. We optimized a number of extrusion process and detail design of inner dice and proper choice of lubricating material, and as a result, the surface roughness in the range of $R_a < 0.8\,\mu$m was achieved, and remained impurities were made quite low. Additionally we decided to use high- quality OFHC (oxide-free high-conductivity copper, ASTM Class-1) material, which costs more than the standard materials, while whose benefit was good enough, i.e., high-power processing was fairly smooth and the rate of high-voltage breakdown during accelerator operation was fairly low (refer to the later sections).

Figure 12 shows the waveguide flange, which electrically connects high-power copper waveguides at the same time seals the vacuum connections (Bizen 2008). We named it as ADESY flange, because of its improved version of conventional flange design used in S-band waveguide around several particle accelerator laboratories in Europe, especially in DESY. The flange is fabricated from SUS316L material, which is bonded to the copper waveguide by means of brazing. Due to high-temperature brazing process (BAg-8: Ag-Cu, 1,080 °C), hardness of the seal edge

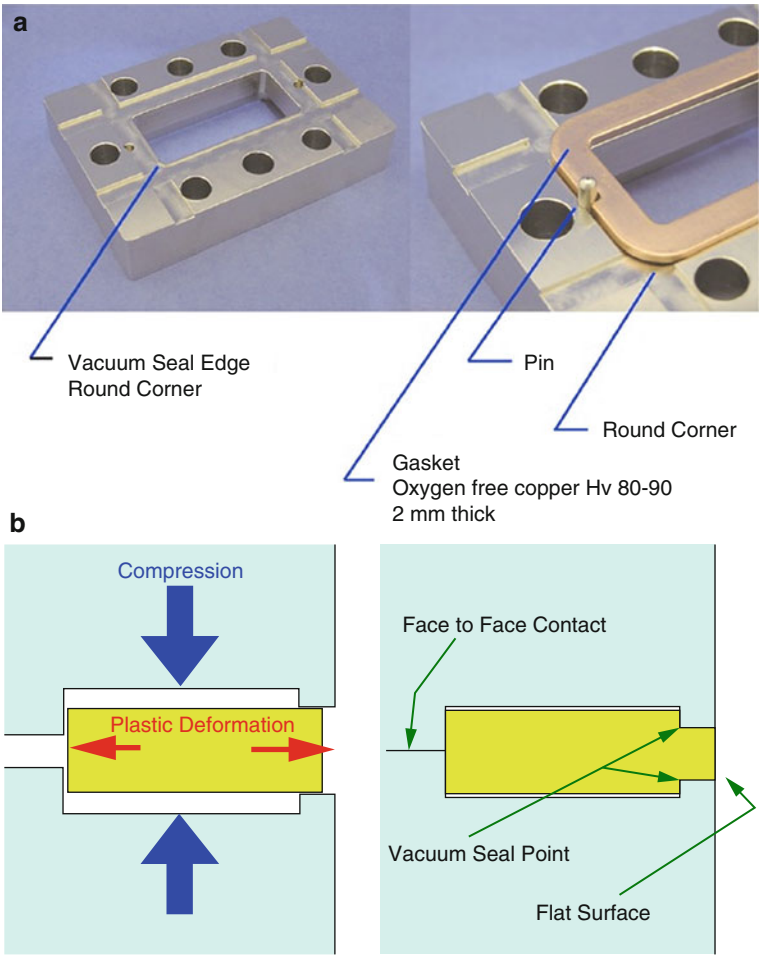

Fig. 12 ADESY-type flange. (**a**) Flange and gasket. (**b**) How gasket works

becomes lower from Hv315 to Hv140, while it does not cause the vacuum leakage. Thickness of the copper gasket was chosen to be 2 mm same as the standard copper gasket for ICF-type vacuum conflate flange, so that we may use the same copper plates prepared for ICF-flange gasket, whose quality is well controlled to meet high vacuum requirements, i.e., the surface roughness, hardness, and cleanness. When we tighten the bolts and nuts, the flange surface at the outer area perfectly touches each other and keeps highly reproducible mechanical dimension. The gasket is designed to be compressed about 30% of its original thickness and creates vacuum seal at the edge corner as shown in Fig. 13.

The compression force on both flanges should be close to the designed value, which is an important factor for reliable handling of flange connections without

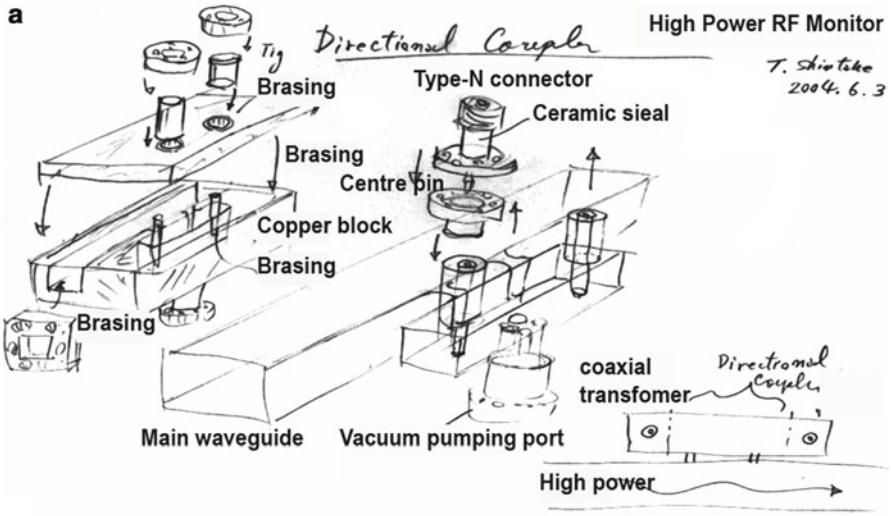

Fig. 13 RF power monitor port and type-N vacuum feedthrough. (**a**) Conceptual drawing of the power monitor port. (**b**) Power monitor port inside the tunnel. (**c**) Type-N vacuum feedthrough

vacuum leak and stable electrical connection to eliminate excess rf losses. For this purpose, the tightening torque on the bolt and nut has to be controlled by using torque wrench, and at the same time, a lubricant has to be applied on the bolt and nut in order to reduce friction loss. The cleaned bolt and nut cause fairly high friction; the friction coefficient is higher than 0.5, and sometimes they are fused to each other after usage. However, commercially available lubricant paste like MoS_2 (molybdenum disulfide) is often a blend of oils and greases; therefore, it will potentially pollute inside waveguide and become a source of the high-voltage breakdown. To avoid these problems, we applied the DLC (diamond-like carbon) coating on all of the bolts and nuts (made of SUS304 stainless steel). Typical characteristics of the DLC coating are (1) higher hardness, HV $= 1{,}000 \sim 3{,}000$, (2), and lower friction coefficient, 0.15 (Bizen 2008).

Along the entire accelerator, a total number of 1,773 sets of ADESY-type flanges were used in the waveguide system. In the construction of SACLA, no

single vacuum leaks were found at 1×10^{11} Pa.m^3/s detection level (with single tightening work, no repeated trial was required). It showed extremely higher reliability.

RF Window

One of the most important components in the waveguide system is the ceramic RF window, which seals vacuum of the output waveguide on the klystron tube. Traditional microwave window normally uses a pillbox-type resonator, inside which a round ceramic disk is used in the middle of the pillbox, which provides vacuum seal. Since the dielectric constant of the alumina ceramic material is as high as 9, which becomes a large capacitive loading on the electrical transmission line, it causes a large microwave reflection. To cancel this reflection, the pillbox cavity dimensions are chosen to resonate at the driving frequency, where the inductive component of the cavity structure cancels the capacitive component; thus, the microwave power can pass through the window without reflection. Because of the resonant nature, a certain amount of the electromagnetic fields is stored inside the cavity structure; thus, the field intensity becomes much higher than that in the waveguide. Most importantly, resonance mode inside the pillbox, which is HEM_{11}-like mode, has longitudinal electric field, which penetrates the ceramic disk in normal direction, and sometimes causes HV breakdown, and, in fatal case, results in a ceramic puncture. This problem had been a long-time running inherent symptom in high- power klystron technologies.

To solve this problem, we designed a long pillbox window, where the reflection wave from the ceramic disk is cancelled with reflections from the waveguide transition between rectangular to circular waveguide (Matsumoto et al. 1997). This scheme is similar to the anti-reflection coating technique commonly used in the optical components to eliminate unwanted reflections from the glass surface, such as lens or laser window. This scheme does not rely on the resonator structure; therefore, no excess field is stored in the window, and especially there is no longitudinal electric field. Therefore, the risk of high- voltage breakdown becomes fairly low. This design has been implemented in the C-band klystrons. Two windows are used in parallel to lower the risk of breakdown. So far 90 tubes were fabricated until today (2014 Summer), and we have not observed any evidence of HV breakdown nor ceramic puncture.

RF Power Monitoring Port

Traditionally monitoring of the rf power flowing inside the waveguide has been performed by directional coupler through a coupling hole prepared on the waveguide top wall (E-coupling), which is sometimes called Bethe-hole coupler. One practical problem in this design is its lower productivity, i.e., the coupling coefficient is fairly sensitive to tiny mechanical changes in coupling structure, for example, which depends on how much torque is applied on mounting screws of the coupler

antenna structure. Thus, production of this type of monitor is a time-consuming work and requires skilled personnel. Even with these efforts, there were sometimes unexpected variations of coupling coefficient that happened during installation or after a long period of operation. Additionally, when the traveling-wave power becomes extremely high, like in our case, there is a certain risk of HV breakdown associated with ceramic window closely located behind the coupling iris of the Bethe-hole coupler. To solve these problems, we developed a directional coupler as shown in Fig. 13, where the power coupling is made by magnetic field (H-coupling) through two slots of $\lambda_g/4$ apart. Advantages of this design are that (1) there is no electric field that exists around the slots (thus the risk of HV breakdown becomes low) and (2) the power-coupling ratio is defined by the slot width and wall thickness, which can be precisely maintained by numerical-controlled lathe machining, and as a result, the coupling ratio becomes fairly reproducible. The secondary waveguide can be attached to the main waveguide by metal brazing or electron beam welding. For the rf-pulse compressor, the hybrid and power monitoring waveguides were fabricated from a single copper block by milling, which made productivity fairly high.

The vacuum feedthrough is also a quite important component to make power monitoring reliable and reproducible. We designed a type-N feedthrough for C-band frequency applications, as shown in Fig. 13. It has fairly low VSWR, <1.1 at 5.8 GHz and <1.2 for DC to 8 GHz. The residual reflection from the feedthrough deteriorates the signal isolation S_{12} parameter of the directional coupler. The isolation in the mass production model was as better as 25 dB. We also used this feed through in beam position monitor cavity. Interior structure and materials are intellectual properties of fabricating company. For more detail, contact to Orient Microwave Co., http://www.orient-microwave.com.

C-Band High-Power Klystron

C-band klystron was developed in the course of C-band R&D for e^+e^- linear collider at KEK during year 1996 $\sim$ 2000. When the author started the R&D, there were no available C-band pulse klystrons at megawatt level. We firstly started to develop copper waveguide and rf windows, and then we could start C-band high-power klystron development.

To design the electrical parameters of the C-band klystron, we scaled it from S-band klystron. For this purpose, we required reliable data on existing S-band klystrons, which should have enough statistics. There were a few models of high-power pulse klystrons at S-band frequency with 50 MW peak power level or higher. SLAC 5045 tube (65 MW peak and 45 kW average output) was one of the best tubes in that period (Jensen et al. 2011), and 245 tubes were used to drive two-mile linac at SLAC. Detailed information of 5045 tube was available, and statistics data of operational performances were also provided as open information. We scaled down the SLAC 5045 tube, i.e., beam cross section to half, while maintaining cathode emission current density as the same value; thus, the beam perveance becomes lower: 1.5 $\mu A/V^{1.5}$ (350 kV, 316 A). In fully utilizing numerical

simulation (FCI: field charge interaction code, particle-in-cell simulation (Shintake 1995, 1996)) of electron beam dynamics, we designed the series of gain cavities, focusing field profile, etc. The first C-band klystron was produced in 1996–1997, and the peak maximum output power reached to the target value of 50 MW at 360-kV gun voltage, while power efficiency was 42%. The tube showed stable and reliable performance, and we did not observe spurious oscillations or high-voltage breakdown inside the tube.

In order to improve power conversion efficiency (we felt 42% was still low) and reduce surface electric field on the output cavity, we designed to employ the three-cell traveling cell output structure (Ohkubo et al. 1998). Figure 14 shows PIC-simulation result using FCI code, which predicted power conversion efficiency as high as 44%, and experimental result showed 43.9%. Importantly, the maximum electric field intensity was reduced from 45 kV/mm down to 29 kV/mm. Because of this, we believe the risk of HV breakdown in this tube to be fairly low. The developed C-band klystron was named as Toshiba E3746, which is shown in

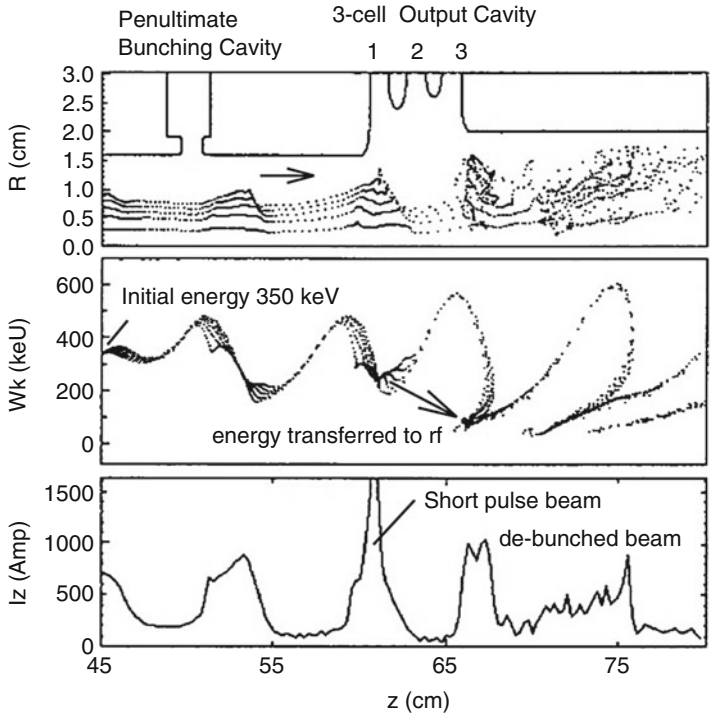

Fig. 14 FCI simulation result on the three-cell traveling-wave output cavity in the 50-MW C-band klystron. FCI simulates beam dynamics after the electron gun down to beam dump. *Top view* is a snapshot of beam cross section (zr-plane), where *gaps* indicate rf cavity cross sections; *middle view* shows electron energy, where we can see the energy-transferring process; importantly there is no back-streaming electrons. *Bottom* is the temporal beam density (current) propagation

Fig. 15 C-band 50 MW klystron

Table 2 C-bank klystron parameter

Operation frequency	5,712	MHz
Peak output power	50	MW
Signal gain	52	dB
Power efficiency	44	%
Pulse duration	2.5	usec
Pulse repetition	60	pps
Gun voltage	350	kV
Beam perveance	1.53	$\mu A/V^{1.5}$
Beam current	316	A
Solenoid focus	4	kW
RF window	Double	Traveling wave
Traveling-wave output	$\pi/2$-mode	3 cell

Fig. 15 and Table 2, and later E37202 with minor change for SACLA project. From year 2011, more than 72 C-band klystrons are running at SACLA for daily operation.

By the way, in the final year of R&D, we tried to develop a tube using PPM: periodic permanent magnet focusing. We hoped to eliminate focusing solenoid coil, its power supply, and associated power consumption. But we failed in this

development due to the beam instability and strong self-oscillations. Space charge field on driving beam (perveance of 1.5 $uA/V^{1.5}$) was still higher than the critical point of beam stability for periodic focusing scheme.

RF-Pulse Compressor (C-Band SLED)

RF-pulse compressor was originally developed at SLAC in order to double the beam energy during SLC project in 1974 (Farkas et al. 1974). That is why it is named as SLED: SLAC Energy Doubler. The principle of operation is as follows: by storing RF energy into resonator cavity with low-loss resonant mode, typically TE_{01n} mode is used, and when the stored energy level approaches to saturation, by quickly reversing the polarity of input RF signal to the klystron (equivalent to shift the phase by 180°), the reflection wave from the coupling iris to the cavity overlaps with the radiating wave from the stored energy, finally producing very high reflection power with interference effect. In principle, it can generate the peak power as high as 9 times as compared to the input power. Using a 3-dB hybrid coupler, we can separate the output power from the input power. Connecting the klystron in one arm of the hybrid coupler at input side and two cavities in the output side, the compressed high power comes out from the neighboring arm to the input side.

Technical issues in RF power compressor are stability of resonance frequency and HV breakdown around the coupling iris. The storage cavity is low loss and high Q; thus the resonance frequency becomes narrow and highly sensitive to the dimensional change (also the temperature change). We paid special attention to maintain the cavity resonance very stable. We designed cavity body rigid and massive by employing thick copper cylinder (thickness ~3 cm) and passing water channels through the wall, where we feed temperature-controlled water with precision better than ±0.1 °C.

The HV breakdown issue has been a well-known problem in SLEDs. If no proper care is taken, dark current flows across the coupling iris at the storage cavity, generating intense X-ray radiation due to electron bombardment inside the vacuum and sometimes causing HV discharge resulting in machine trip. The physical origin of this problem is the extremely high surface electric field around the coupling iris. To avoid these phenomena, we have to reduce electric field as much as we can. In our design, we used four-hole mode converter as shown in Fig. 16, where we could reduce the peak power density four times and the electric field intensity two times (Shintake et al. 1997b). In addition, we employed thick cavity wall at the coupling iris, which also contributed to lower the field intensity. Because of this design, the high-power processing and nominal operation were fairly smooth. Machine trip related to the rf-pulse compressor is negligibly small in practical operation.

Table 3 summarizes the parameters. The storage cavity uses $TE_{0,1,15}$ mode, where z-index 15 means there exists 15 half waves (antinodes) along z-direction. Because of high z-index, the spectral density of the resonant modes is very high, and thus there is a risk of mode mixing and enormous energy loss. This is the

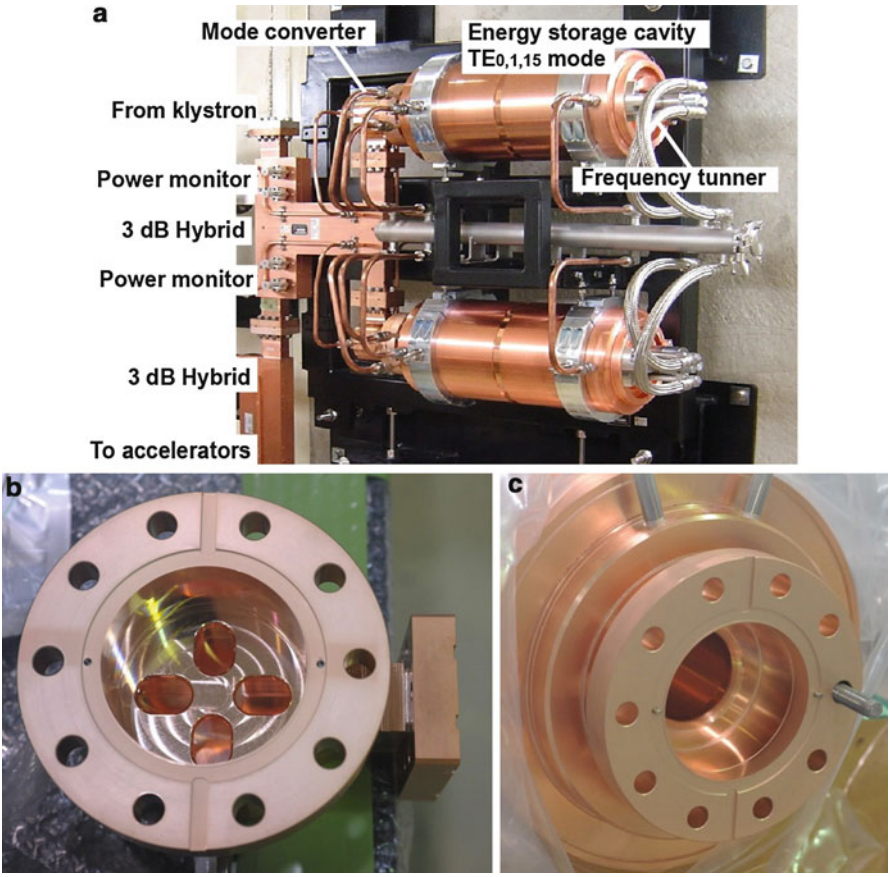

Fig. 16 RF-pulse compressor. (**a**) Configuration of C-band rf-pulse compressor; (**b**) the mode converter uses four coupling holes, which makes electric field intensity lower; (**c**) coupling hole to the cavity is designed wide and rounded, reducing risk of HV breakdown and also providing higher vacuum pumping speed

Table 3 Parameter of the rf-pulse compressor

Resonant frequency	$5,712 \pm 0.02$ MHz
Resonant mode	$TE_{0,1,15}$ Cylindrical
Unloaded Q-factor	185,000
Coupling constant β	8
VSWR	<1.1
Power gain (average gain over filling time of 300 ns)	4

reason why we prepared the mode converter, i.e., which converts the TE_{10} mode of the incoming rf power from the klystron to the circular TE_{01} mode, followed by circular waveguide and coupling to the cylindrical cavity. With this scheme, we

could eliminate parasitic coupling through TM- or TE_1-like modes. In addition to this, inside the cavity a groove structure was also prepared to separate degenerated mode frequencies for TE_{01} and TM_{11} mode.

Residual frequency error after machining of the cavity is around ±500 kHz, which is much larger than the required tuning tolerance. Therefore we need a mechanical tuner, which has to be carefully designed to meet the tuning range/resolution and also stability. We employed differential screw as shown in Fig. 17, which is the same mechanism as used in commonly used micrometer adjuster, by which we could control resonance frequency in 10 kHz (1 μm) precision. This resolution is enough for frequency precision required for tolerance 5,712 ± 0.02 MHz to maintain the rf compression gain maximum and to minimize the rf reflection back to the klystron.

Sixty-four sets of the rf-pulse compressor were manufactured in an industry located in Kobe, Japan (Okihira et al. 2011). The storage cavities, the mode converters, and the 3-dB hybrid couplers were made of OFHC (oxide-free high-conductivity copper) and were assembled with the metal brazing. After assembling, the rf properties, such as the resonant frequencies, Q-factors, and the coupling constant, were verified by using the rf network analyzer. Tuners were adjusted for the resonant frequency within ±20 kHz to meet the required voltage standing wave ratio (VSWR) less than 1.1.

During high-power operation, the resonant frequencies were finally adjusted by controlling the cooling water temperature. The operation temperature was designed to be 30.0°, while some compressors needed to be operated at slightly higher temperature. Figure 18 shows the amplitude of the output of the four rf-pulse compressors as a function of the cavity temperature. The cavity temperature is regulated within ±0.02°C around the optimum temperature, in order to reduce rf output amplitude variation below 0.1%.

Figure 19 shows the typical waveforms of the rf powers and a high voltage applied to the klystron. The high-voltage pulse has a width of 4.5 μs in FWHM

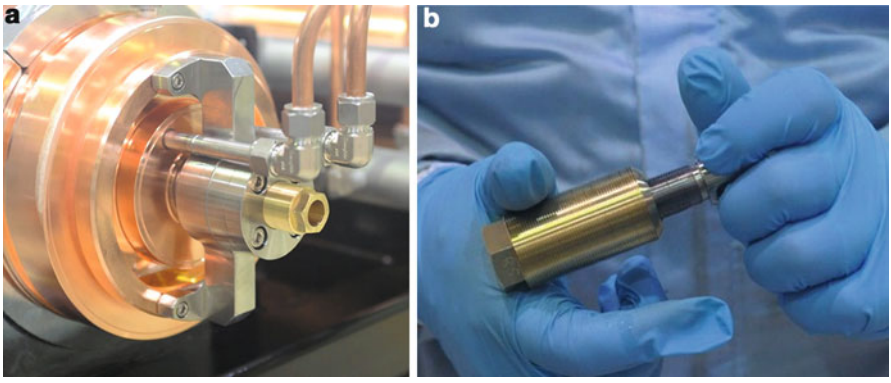

Fig. 17 Frequency tuner. (**a**) Tuning is made by pushing/pulling the end plate; (**b**) tuning screw with differential threads

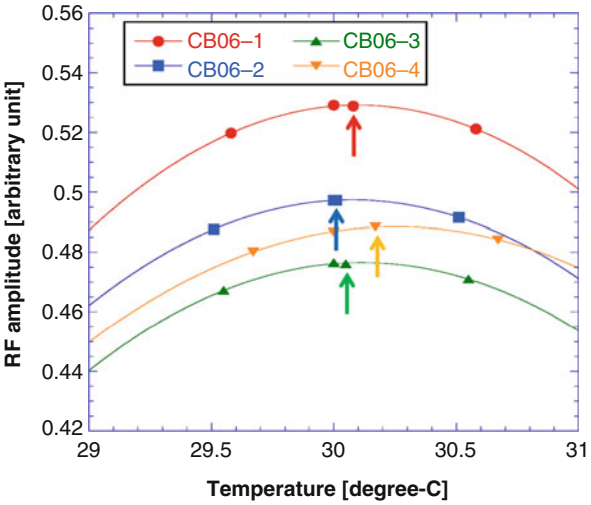

Fig. 18 RF-pulse compressor outputs as a function of the cavity temperature in four sets of C-band acceleration units, named CB06-1, CB06-2, CB06-3, and CB06-4. The curves are the quadratic fit on the measured data. The *arrows* indicate the optimum operation point

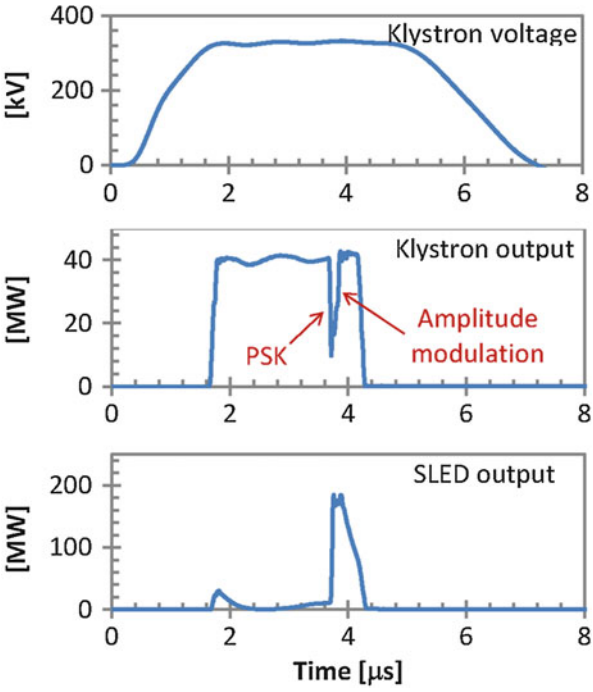

Fig. 19 Typical waveforms of the klystron gun voltage, the output rf power from the klystron, and the rf-pulse compressor output. This figure is a case of an acceleration gradient of 38 MV/m

to obtain a flat top of 3 μs. The pulse width of the klystron output is 2.5 μs. Flipping the phase by 180° at 2.0 μs, we obtain compressed pulse of 0.5 μs width, which is enough length for rf filling time to C-band accelerating structure and passing the beam pulse.

The spiky sharp peak on the triangular waveform of the output pulse is a potential source of high-voltage breakdown inside accelerating structure. To reduce the risk, we applied amplitude modulation by LLRF system to flatten the rf-pulse compressor output, as shown in Fig. 19. The amplitude modulation effectively reduces the peak power at the spike from 250 to 200 MW, while the amplification factor of 4 by the rf-pulse compressor is still maintained (because of lowering output peak and saving usage of stored energy inside the cavity, as a result, it is able to maintain pulse height flat and longer).

Compact Klystron Modulator Power Supply

Among various hardware components required for the electron linear accelerator, the pulse power supply for the klystron tube, called pulse modulator or simply "modulator," is one of the most expensive and troublesome components. Success of klystron modulator operation is essential to the project. The physical origin of the difficulty is related to extremely high-peak power requirement to drive klystron generating high-peak microwave power for the beam acceleration. Generally speaking, a few megawatt (MW) peak power is rather easy to handle. For example, in small medical accelerators, this level of the rf power is frequently used and its technology has been well established. More than 30-MW level is commonly required in S-band electron linear accelerators for academic researches; therefore, it is believed that the technology around the modulator is well established. However in reality, the klystron modulators are still unreliable sometimes. In case of X-ray FELs, extremely high uptime operation and stable beams are required for the linear accelerator; therefore, we have to carefully analyze currently available technology and perform optimized design.

SACLA employs 72 units of the modulator power supplies to drive the klystrons and the electron gun. We took the following guideline: use the same components for all klystron power supplies at different frequencies ranging from L-band to S-band to C-band required in SACLA, which makes maintenance easier. To guarantee reliable operation, we made machine design to minimize the EM radiation from the switching thyratron tube and isolate interior circuit from environmental temperature and moisture change; we housed all the PFN circuitry and high-voltage pulse transformer into one metallic enclosure and filled with insulation oil and cooled by the water. Because the insulation oil has much higher threshold for corona discharge than air, we could make the modulator compact, which is suitable for the C-band high-gradient accelerator.

Modulator Circuitry

Figure 20 shows the circuit diagram. We employed conventional line-type pulse modulator: PFN (pulse-forming network) and step-up pulse transformer. As already shown in the diagram of the operation cycle in Fig. 9, in each cycle, firstly, the switching power supply charges PFN capacitors up to 50 kV, followed by triggering

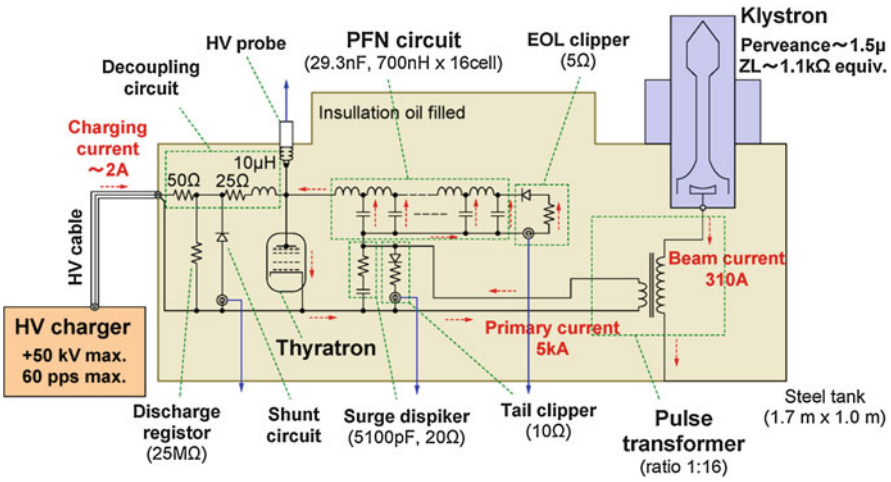

Fig. 20 Schematic diagram of the klystron modulator. It consists of the conventional line-type PFN circuit, thyratron, and pulse transformer; all of them are installed in the metal tank filling with insulation oil. The klystron is mounted on top of the tank, which forms a part of the shielding box. The DC power is supplied from a HV charger siting outside

Table 4 Specifications of the klystron modulator

Maximum charging voltage	50 kV
PFN circuit capacitance	470 nF (29.3 nF × 16)
Pulse width (FWHM)	4.5 μs
Flat top width	3.0 μs
Output voltage/current	350 kV/320 A
Output peak power	110 MW
Maximum repetition	60 pps
Thyratron tube	CX1836 Deuterium filled
Mechanical dimension	1.7 × 1 × 1.2 m
Insulation oil	IEC 60296 transformer oil
Total weight	4.5 ton

and turning ON the thyratron tube to generate a square pulse, length of 4.5 μs, and voltage of 25 kV, which is connected to the primary winding pulse transformer; finally a 350-kV pulse is fed into the klystron cathode.

All of the high-voltage components, the PFN circuit with 16 capacitances and 16 inductances, the thyratron tube, the pulse transformer, and protection circuits, are installed in one tank filled with insulation oil. The line-type modulator circuitry has matured through long period of experience in the accelerator applications since 1960, when the first large-scale electron accelerator was built at Stanford University. Table 4 summarizes the specification of the modulator. The charging voltage of 50 kV and the winding ratio of the pulse transformer of 1:16 are determined based on the availability of the thyratron tube as well as the impedance of the klystron.

The PFN circuit comprises of 16 series network of the capacitor (29.3 nF) and the inductor (700 nH), which form a delay line. Its round-trip delay is designed to be 4.5 μs. We employed the metalized film capacitor from General Atomics (PDS series fast-pulse capacitor), capacitance 0.0293 μF + −2.5%, voltage rating 50 kV, having a lifetime longer than 10^9 shots, which corresponds to 5 years of operation at 60 pps. It's design is the double-ended plastic case capacitor, with an axial terminal arrangement, internally configured for very low inductance. We did not choose self-healing capacitor because of its higher heat loss associated with higher resistance of thinner metal coating and higher field gradient across insulation film.

The characteristic impedance of the PFN circuit, given by $Z_{\text{pfn}} = \sqrt{L/C} \sim 4.9\,\Omega$, has to match with the beam impedance of the klystron through the pulse transformer, given by $Z_L/n^2 \sim 4.3\,\Omega$, where n is the step-up ratio of the pulse transformer: $n = 16$. The PFN impedance is designed to be slightly higher than the klystron; thus there is a negative reflection of −6% amplitude (its power loss is negligibly small), which provides a small reverse voltage on thyratron after the pulse to extinguish the plasma remained inside the tube.

We eliminated the core bias circuit, which has been commonly used in many modulators to reset the remanent field and avoid core saturation after a series of pulse operation. However, the core bias circuit was a source of noise leakage and also troublesome hardware; since a DC power supply has to be connected to the primary winding of the pulse transformer, even though a series choke inductor was used, the power supply was sometimes interrupted with high-voltage pulse leakage, also creating a large noise to the environment. We employed gap core and inserted an insulation foil of 200 μm between two cores, which made remanent field smaller than 1 kG; thus the core bias circuit became not necessary.

In order to charge energy into the PFN capacitors, we employed the solid-state high-voltage inverter charger. Since it runs at fast switching frequency as high as 20 kHz, the step-up transformers become quite small as compared to the transformers for AC line frequency 50 ∼ 60 Hz (low-frequency transformer requires a large inductance). There were several commercially available inverter-type high-voltage chargers in this power range. However, their voltage regulation was not good enough for the X-ray FEL application, i.e., the residual voltage jitter was on the order of 0.1% associated with the single charging cycle of the inverter circuit. This voltage jitter is the largest source of the pulse-to-pulse fluctuation of the amplitude and phase of the accelerating rf field. The X-ray FEL requires much better stability on the order of 0.01%; therefore we needed to develop a custom -designed high-voltage charger (refer to the later sections).

Thyratron Tube

In the modulator circuitry, proper choice of the high-power switching device is the most important key to develop a reliable modulator. We chose the traditional "thyratron tube," which relies on hydrogen gas discharge as active switching

medium. Thyratron can switch high voltage (up to 100 kV) and high current (a few kA) with very fast turn-on speed (<100 ns) and extremely low impedance (<1 Ω) at conduction mode. Additionally, it is fairly robust against over voltage, over current, or klystron gun spark; therefore this device has been widely used in high-power switching equipment, lasers, plasma generators, and electron linear accelerator including medical and scientific applications. We use a deuterium gas-filled two-gap thyratron: CX1836 from E2V, maximum rating voltage 50 kV, current 10 kA, average current 10 A, and repetition cycle 10 kHz.

The thyratron tube has inherent self-hearing mechanism. In each operation cycle of discharge, the switching medium of gas causes "breakdown," while it is fully recovered by feeding fresh gas molecules from reservoir and nothing remains changed. Gas discharge takes place in a gap between two parallel electrodes (normally made by copper with molybdenum surface layer), which are robust enough against ion collision. By triggering voltage on grid, the driving electron beam is generated from cathode, which ignites a plasma discharge. The cathode is located behind a potential electrode, and there is no direct path for ions to collide to the cathode; thus the cathode (delicate component) is protected safely.

One drawback of the thyratron tube is that the switching action always shows certain fluctuations, i.e., turn-on delay time, rise time, fall time, and also turn-on impedance are changing slightly pulse to pulse or drifting over time. For a long period of operation, it shows substantial aging effect. After a few years of operation, fluctuations are getting bigger and bigger, and finally when we see frequent high-voltage breakdown (self-firing), we need to replace it. Generally speaking, lifetime of thyratron (2 or 3 years) is relatively shorter than other devices in the accelerator, such as, klystron tube (average lifetime is more than 5 years now).

To maximize the lifetime, uniform plasma generation in the tube is essential. If it is not uniformly created, the plasma impedance becomes higher, and thus higher energy electron/ion collides to electrodes, which cause sputtering and depositing metals on the insulation ceramics, resulting in frequent self-discharges. For maximum cathode utilization, we followed the manufacture recommendations on two-trigger pulses and negative bias on grids [e2v]. It costs more on the triggering circuitry, but we believe it is beneficial to maximize tube lifetime.

We knew our design was somewhat out-of-date, but the solid-state switch was not mature to drive 50-MW klystron when we started the design of SACLA accelerator in 2001. Today's trend is introducing more solid-state switches, such as IGBT, insulated-gate bipolar transistor. Even automobile engines are now replacing with the electric motor and the lithium-ion battery, in which the feeding power is controlled by IGBT switching circuit. Reasons of this trend are because of its superior efficiency and simple mechanics and because it is environmentally friendly than the traditional reciprocal engine using fossil fuels. It produces great industrial needs on related technologies; thus the solid-state switching device is advancing day by day. Today (2014), modern IGBTs have reached switching maximum capability of a few kV and a few kA, with sufficiency turn-on speed (<0.5 μs). It is reasonable to say that the solid-state modulator will be a correct choice from now for the next-generation accelerator applications. One big issue in using solid-state device

in high-power and high-voltage application is the accumulation of interior damages around the junction. Once a high- voltage breakdown has occurred through cathode-to-anode zones in IGBT, it cannot recover until we replace it with new switch, i.e., there is no self-healing effect in the solid-state devices. Therefore, risk management will be the major task in solid-state modulator.

PFN: Pulse-Forming Network Block

In traditional PFN circuit design, tuning plungers were commonly prepared to adjust the series inductances in LC network in order to provide output waveform having a flat top within certain tolerance. However, the mechanical design of plunger was fairly troublesome, and heat loss due to induction current on the short plunger was fairly large; thus its cooling was also an issue. We eliminated the tuning mechanism from the PFN due to the following reasons:

1. To make the PFN block as a simple design, lowering the cost and also more reliable.
2. To eliminate excess heat generation in the PFN circuit.
3. Output voltage to the klystron gun is not necessary to be a very flat waveform, because the rf power from the klystron is fed into the rf-pulse compressor, where the waveform distortion does not affect to the compressed output power. If there is no pulse-to-pulse fluctuation, a certain variation on the klystron voltage is acceptable. From the practical requirement on testing klystron and related devices, we defined flatness requirement as 3% p-p on the flat top.

We designed a simple PFN block, which uses simple coils as PFN inductor without tuning plungers as shown in Fig. 21. The number of the windings was determined by iteration on a numerical simulation (trial and error on a computer). In principle, a PFN circuit (LC delay line) connected to a simple resistive load generates a square output wave to the load. There is a small distortion at rising part due to wave dispersion effect associated with the lumped LC circuit, while it is negligibly small. Why the tuning plunger is normally required? The reason is that the load is not a simple resistor; in practice it is the beam impedance looking from the first winding of the pulse transformer. Additionally, the transformer and klystron cathode have a large amount of parasitic capacitances around 160 pF, which cause overshoot phenomena in combination with leakage inductance in the transformer (Oh et al. 1997). To compensate this, the tuner plungers are normally prepared on the series inductors.

We performed a number of numerical simulations with different set of inductances. By automated iteration process, try waveform simulation with a set of inductances and try again with increased/decreased number of windings in some inductance, and by comparing waveforms, a better solution was chosen; after repeating many cycles, the optimum number of windings was found to

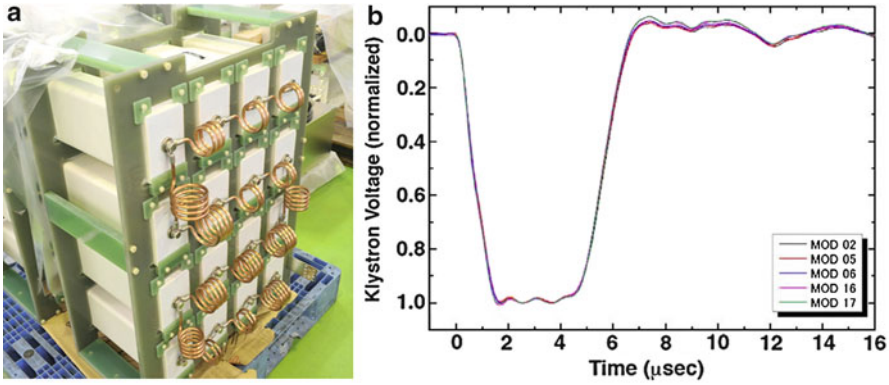

Fig. 21 (**a**) The PFN block in the mass production. The series inductors were optimized by numerical simulation. The identical coils were used in all modulators. The capacitance values of the high-voltage capacitors (29.3 nF) were almost constant within 1% error. (**b**) Example of the output waveforms from five modulators

all inductances. In the mass production of modulators, output waveforms were reproducible and within our specification, without tuning the inductance.

Pulse Transformer

The pulse transformer is basically the traditional twin coil design, while coils are made by epoxy molded for better rigidity and reproducibility. The first winding is 7 turns of 5 parallel copper wires, the second winding 112 turns of single wire; the step-up ratio is 1:16. At 50 kV charging voltage on PFN capacitors, the output voltage becomes 350 kV (including reflection loss). We used JFE Super core (non-oriented 6.5% Si-Fe) of 100 μm thickness as the core material. It is known that the magnetostriction of steel becomes zero at 6.5% Si doping level, and also the eddy current loss becomes very small due to high electric resistivity. However, magnetic saturation level becomes as low as 1.5 T, which is much lower than that of the highly oriented steel: 1.8 T at the magnetization of 800 A/m. Thus we needed to employ wider core cross section: 129 cm^2, as shown in Fig. 22.

As mentioned in the later section on the electromagnetic shielding, we eliminated the core bias circuit, which had been commonly used in the pulse transformer to make the flux swing close to twice higher than the saturation level, or demagnetize the remanent field. However, it was also a huge noise source to the environment, since it was directly connected to the first winding of the pulse transformer, and sometimes caused circuit malfunction in the DC power supply for the bias current. To do so, we employed the gap core design: attaching two C-shape cores with a gap spacer in between, making effective magnetic permeability much lower; thus the remanent field becomes negligibly small. We inserted 100 μm glass epoxy sheets in the gap. The estimated remanent flux was lower than 1 kG with the total gap length

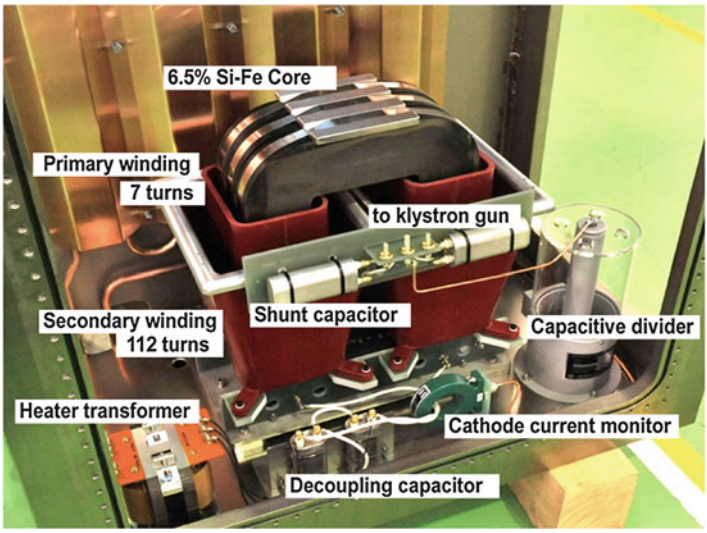

Fig. 22 The pulse transformer for C-band klystron. The coils are made with glass epoxy molding. The bias circuitry was eliminated for resetting the remanent field in the core; instead the gap core was employed

200 μm. As discussed in frequency scaling of the accelerating system, if we try to do high-gradient acceleration with S-band system, the required pulse energy per klystron becomes at least four times higher (four times flux swing in the core); thus the bias circuit will be required.

During mass production of the transformer, a technical problem happened at core production process. It was found that the electrical insulation was not enough between steel sheets inside the core material, and some of them had electrical shortage between layers. If it was used in the high-power modulator, it could cause energy efficiency degradation due to impedance mismatching or high- voltage sparks at the gap core due to magneto induction. There were two sources of the problem: first the core cutting process (making C-core) caused electric short at cutting surface, and second the insulation coating on 100 μm-steel tapes was not high-temperature resistant and thus was damaged during the annealing at 400 °C. These problems were solved by electrical etching on cutting surface, followed by sintering with epoxy resin.

The original idea for using 6.5% Si-Fe was to improve speed of rising and falling time of the output pulse and lowering eddy current loss. However, since the saturation field was lower, we needed larger core volume, which made the leakage inductance between windings larger, and as a result, rise and fall times did not improve. The heat generation seems lower but not evident. As a conclusion, it is reasonable to say that 6.5% Si-Fe core is not suitable to pulse transformer applications requesting a large output voltage. The traditional 3% Si-Fe-oriented steel core will be the best choice among currently available technologies.

Electromagnetic Shielding and Modulator Tank Design

Klystron modulator switches high voltage stored in the PFN capacitors to generate a huge peak power in a few microseconds. Voltage swing across thyratron tube is extremely fast: 50 kV/200 ns and 350 kV/μs on the klystron tube. It radiates a huge electromagnetic noise into wide frequency range up to a few 10 MHz. Therefore, proper management for electromagnetic shielding is highly important to protect highly sensitive control circuits inside the accelerator and also protect nearby residence from EMI (electromagnetic interference) problem.

Figure 23 shows concept of electromagnetic shielding. Ideally if we enclose the switching circuit by a perfect conductive boundary, the electromagnetic fields cannot escape from the boundary. This is known as Faraday cage, which gives basic ideas of the electromagnetic shielding. However, in practice, we need to feed electric power into the interior circuit and bring out monitoring signal to the outside. To do so we need to prepare holes and connection cables. Along these cables, the electromagnetic radiation leaks out. The shielding box should have the access hatches to maintain interior circuits, where the electromagnetic radiation also can leak through gaps around the access hatches. Therefore, proper electromagnetic shield design should:

1. Make the housing box as close to Faraday cage
2. Stop noise propagation along the cables at Faraday cage boundary

To meet these requirements, we developed the modulator tank as shown in Figs. 24 and 25, in which all of the modulator circuitries are housed (Shintake 2010). The klystron is mounted on top of the tank, and its cathode electrode is directly connected to the secondary windings of the pulse transformer sitting below. We

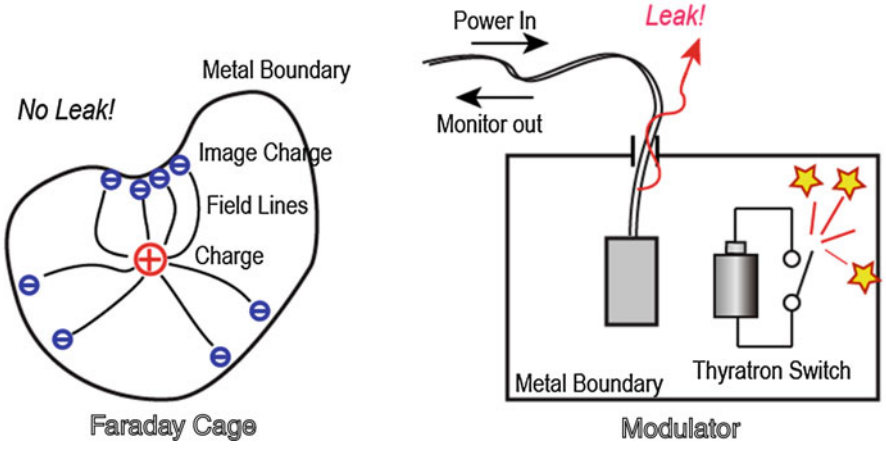

Fig. 23 Faraday cage concept for electromagnetic shielding design. Practical modulator needs cable connections

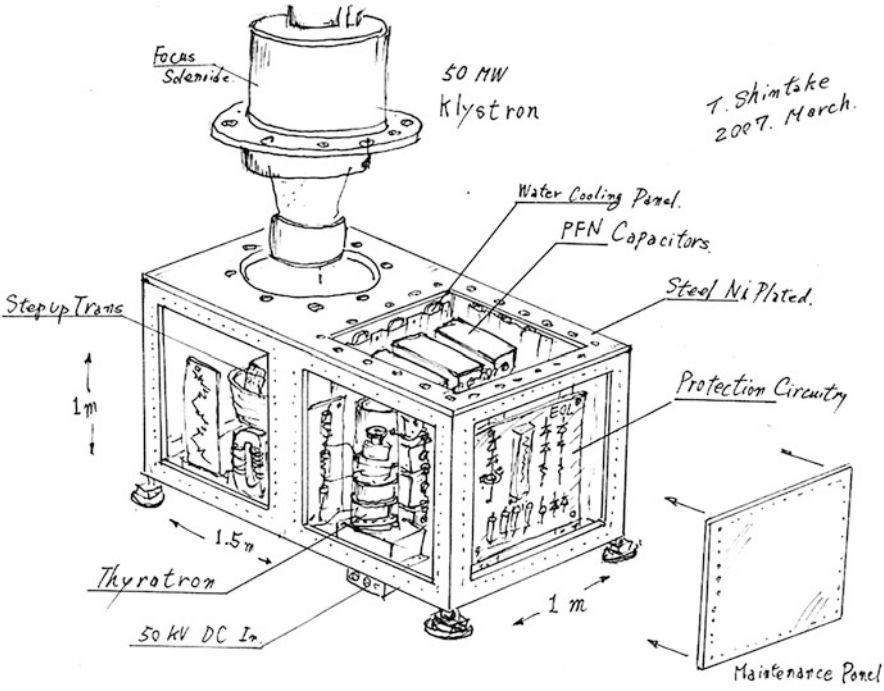

Fig. 24 Conceptual drawing of the single tank modulator

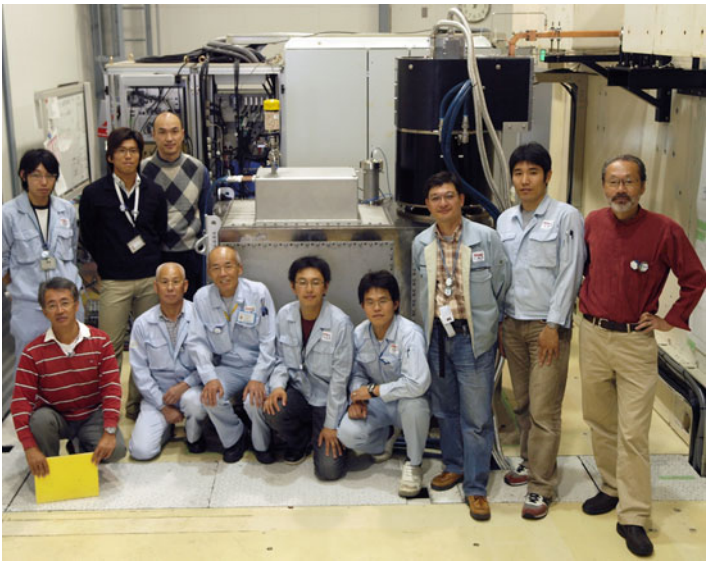

Fig. 25 The first prototype of the single tank modulator and contributors on October 2008

could eliminate the triaxial high-voltage cable, which was traditionally needed to connect the modulator and klystron and one of the most troublesome components, i.e., it sometimes causes high-voltage breakdown between coaxial shields, and additionally it takes a quite long production time since it is a custom-made item, and normally a cable company only accepts production for a certain volume like 1 km. Therefore, eliminating the triaxial cable was an important key to accomplish our project as scheduled time line.

The modulator tank is made by steel with Ni plating for rust protection and better electrical contact. Firstly, steel plates were cut by plasma jet, the surface was machined and welded together with grooves for O-rings and female screw threads were machined on a digital controlled lathe, and finally Ni plating was made on the whole surface. One can also use stainless steel to make a tank since it does not require rust protection. However, temperature rise and mechanical distortion become larger; thus annealing process will be required, which costs more.

The shield box has several hatches for assembly and maintenance. We filled the transformer oil for the high-voltage insulation and also removed heat from the components. The major heat sources are the cathode heater of the klystron, the pulse transformer, and the thyratron tube. Total heat was estimated to be 3 kW at maximum. We prepared four water-cooling panels in PFN side, one for klystron side as shown in Fig. 26. The cooling panel has quite high thermal conductivity to the oil as high as 130 W/m^2K (Kondo et al. 2008). Heated oil rises up due to thermal expansion and, cooled by the water-cooling panels mounted on the maintenance hutches, causes natural convection inside the tank. Using cooling water temperature of 30 °C, the oil temperature during operation is well regulated below 45 °C, which is a key to stabilize the thyratron performance and also lengthening its lifetime.

To supply AC power to the heaters in the klystron cathode, the hydrogen reservoir, and the cathode in the thyratron, we need cable connections from outside the tank. Unfortunately, they break the boundary of Faraday cage and bring out the thyratron switching noise. We need noise filters at the Faraday cage boundary. Since AC power is transferred as a differential voltage/current across two electric-conducting lines, normally they are formed as parallel lines (pair lines), not as coaxial cables. When the thyratron switches, +50 kV voltage on the anode electrode suddenly drops to ground potential and associates rush current flows around the thyratron tube, which also creates magnetic flux noise. If we use twisted pair lines inside the tank, the magnetic fluxes between two lines are cancelled in each twist. Therefore, only the electric field coupling induces noise voltage on the pair lines, in the same polarity; thus it is called common-mode noise. There exist commercially available common-mode choke filters, while they are mostly designed for small noise applications. When it is used in the klystron modulator, the magnetic core inside the choke filter will be saturated, and filtering function will be lost. Figure 28 shows our custom-made filter. A high permeability amorphous core is used, and it can isolate 1 kV × 0.5 μs pulse voltage between input and output sides. It is a coaxial hermitic design, using O-ring seal, basically LC π-filter circuit. Filtering gain was achieved as high as 60 dB at 1 MHz or higher frequency.

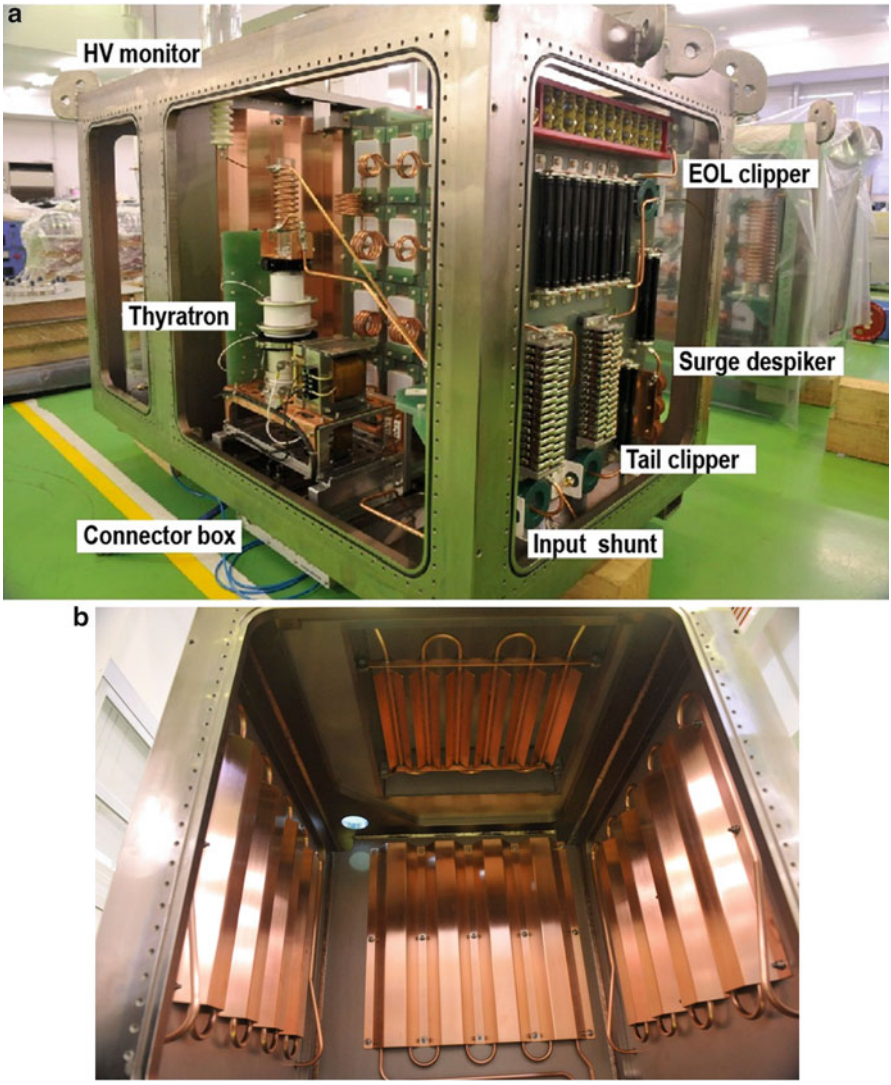

Fig. 26 Interior view of the klystron modulator. (**a**) The modulator tank is made by steel with Ni-plating for rust prevention and better electrical contact. The protection circuitry is mounted on glass-epoxy board, thus maintenance is easily. (**b**) Four cooling panels were used to remove heat from insulation oil (transformer oil). Since viscosity of the oil is fairly high, and the speed of flow of natural convection is slow, thus a large area is necessary for heat exchange for expected heat generation of 3 kW (Kondo et al. 2008)

There are also several coaxial cables required for monitoring klystron gun voltage monitor, pulse current monitor, etc. They do not carry much noise to the outside, because we can make the coaxial cable as a part of Faraday cage. To do so, we use semirigid copper cables inside the tank and terminate the outer shield at the Faraday

Fig. 27 (**a**) Mass production of the modulator in a factory. (**b**) Transportation and installation of klystron at SACLA site

cage boundary by using panel J-J adapter as seen in the right side of Fig. 28b. The induced noise voltage on the outer shield remains inside the tank and cannot escape from Faraday cage.

Thanks to all those detailed efforts, EM noise leakage was made extremely low. We could nicely listen AM radio right next to the modulator when it was operating. Actually, the fluorescent lamps in the experimental room were higher source of EMI noise to the AM radio than the modulator.

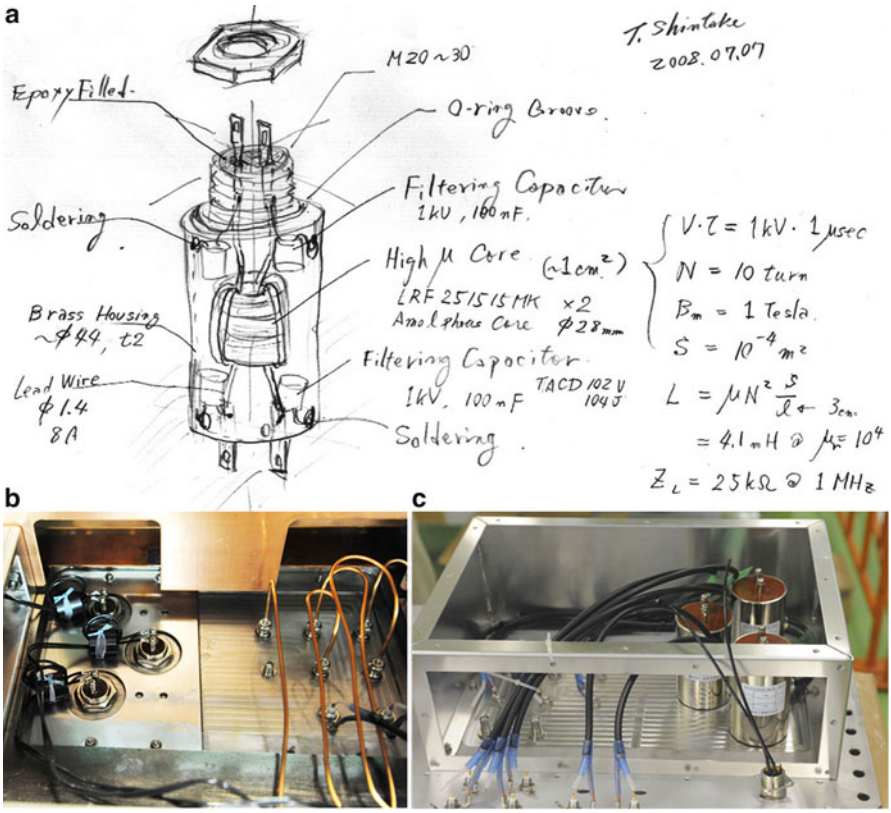

Fig. 28 Coaxial hermetic common-mode filter. (**a**) An amorphous core (AL18 μH) is used in the choke inductance, which will not be saturated for a large noise pulse as high as 1 kV × 0.5 μsec; (**b**) the filters were assembled at the bottom of the tank, and (**c**) filter bodies are housed in a cable connection box

The steel tanks have enough mechanical strength; thus all electrical components were assembled at the factory located near Kyoto, and then the modulators were transferred to SPring-8 site through 200-km highway by using a truck with air-suspension as shown in Fig. 27. One of the issues during this transportation was mechanical vibration on the thyratron tube. We performed vibration measurement using an accelerometer inside an empty steel tank and drove through the scheduled route. This experiment showed that the maximum acceleration was well below than the specified guarantee level of the thyratron tube. The klystrons were assembled at SACLA site.

Switching Inverter HV Charger for PFN Capacitor

Figure 29 and Table 5 show the circuit diagram of the high-voltage charger and the electrical specification. It uses two charging circuits connected in parallel: the main

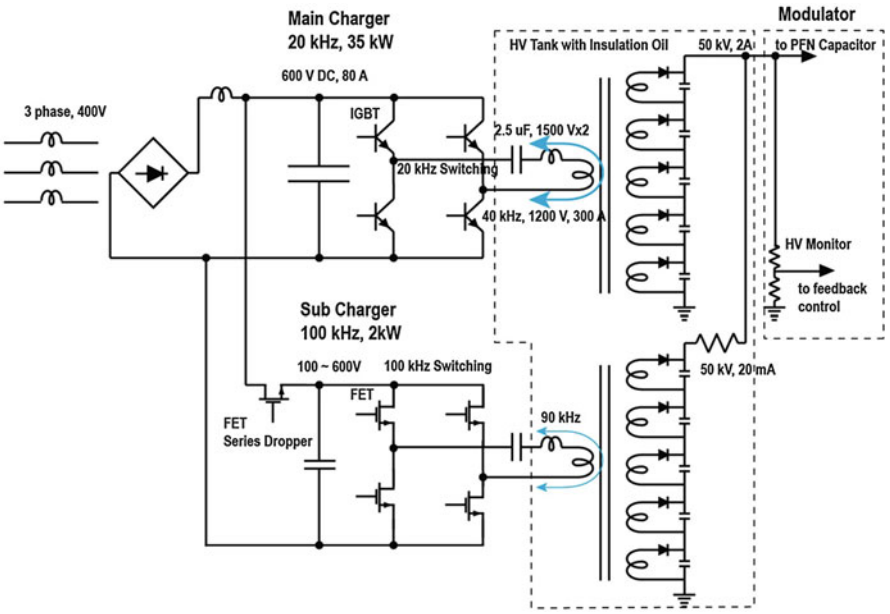

Fig. 29 Circuit diagram of the high-voltage PFN charger, which consists of two charging circuits: a main charger and a sub-charger, in parallel connection. After the main charger fills high voltage, the sub-charger trims the charging in high precision

Table 5 Specifications of the high-voltage charger

Maximum charging voltage	50 kV
Charging current	Main charger: 2 A
	Sub-charger: 20 mA
Maximum output power	36 kW
Maximum repetition	60 pps
Power efficiency	87% (50 kV, 60 pps)
Power factor	87% (50 kV, 60 pps)
Charging voltage stability (standard deviation)	(pulse to pulse) 0.001% (10 ppm) (long term) 0.03% (300 ppm)
Size	19-in. rack mount, $0.4 \times 0.6 \times 1.4$ m

charger and the sub-charger. The main charger has a high-power charging capability with a full-bridge four IGBT's (insulated-gate bipolar transistors), which generates square wave voltage at 30 kHz of 600 V, which drives the step-up transformer to generate 50 kV in the second windings. To compensate the phase delay due to the leakage inductance in the transformer and improve power conversion efficiency, between the IGBT's bridge and the first winding of the transformer, a compensation capacitor is inserted (sometimes called resonant capacitor). The choice of this capacitor (2 μF, 1,500 V) and the circuit arrangement are technically critical issues,

because full charging power has to be transferred through this capacitor at high frequency (40 kHz); thus it generates heat. The cooling of the charging capacitor becomes a big issue. In order to minimize heat loss, careful designs were made to lower the inductance and resistance throughout the circulating current along the capacitor bank in DC line, IGBT, the resonant capacitor, and the first winding of the step-up transformer. Those entire components are housed inside a metal shielding box filled with insulation oil, whose heat is removed by a water-cooled heat exchanger.

In one cycle of operation, at first, the main charger generates a charging current of 2 A, which quickly charges the PFN capacitors until the charging voltage reaches to 99.7% of the target value within 12 ms, followed by starting the sub-charger to fill the remaining voltage up to the target voltage. The sub-charger has much lower power capacity, which runs at higher switching frequency (near 100 kHz) than the main charger (20 kHz) to minimize the charging bucket size. The field-effect transistors (FETs) are used in the full-bridge switching circuit. The charging current is controlled by a series voltage dropper using FET in front of the FET switching circuit, which is controlled by the feedback signal from a voltage monitor on the charging voltage. To achieve higher precision and pulse-to-pulse stability, finer charging current in sub-charger is required, which reflects back to the requirement on the main charging control to be accurate and fast. We developed high-precision fast- voltage monitor (refer to the later section).

Figure 30 shows the typical waveform of a charging sequence of the high-voltage charger and modulator. The stability of the charging voltage is precisely analyzed by a high-resolution oscilloscope through a differential amplifier. The short-term voltage jitter was measured to be about 0.001% (10 ppm) in the standard deviation. It causes rf-field amplitude and phase fluctuations of only 0.0013% and 0.005° in the acceleration structure, respectively.

For more detail on this power supply, please contact directly to Nichicon Co. (http://www.nichicon.co.jp).

High-Precision Fast-Voltage Monitor (Resistive Divider)

One technical problem of the high-voltage monitor (resistive divider) is the relativity slow settling time, typically 1 ms for 50 ∼ 100-kV monitor. This is due to extremely high resistance value used on the high-voltage side divider, as high as 1 GΩ. Since the mechanical size of the high-voltage resistor is quite large (10 mm in diameter and 200 mm long for 50-kV monitor), it forms distributed RC delay line associated with the parasitic capacitance. Traditionally, capacitive compensation circuit is used to cancel the longitudinal parasitic capacitance effect (sometimes called the pole-zero cancellation), while there are parallel capacitances associated with transverse electric field, which causes a large amount of phase delay even at low frequency, resulting in slow settling time. If it is used as a feedback loop of a pulse power supply, this phenomenon causes a serious problem. An overshoot or undershoot swing appears in the monitor signal, which will limit the settling time of the

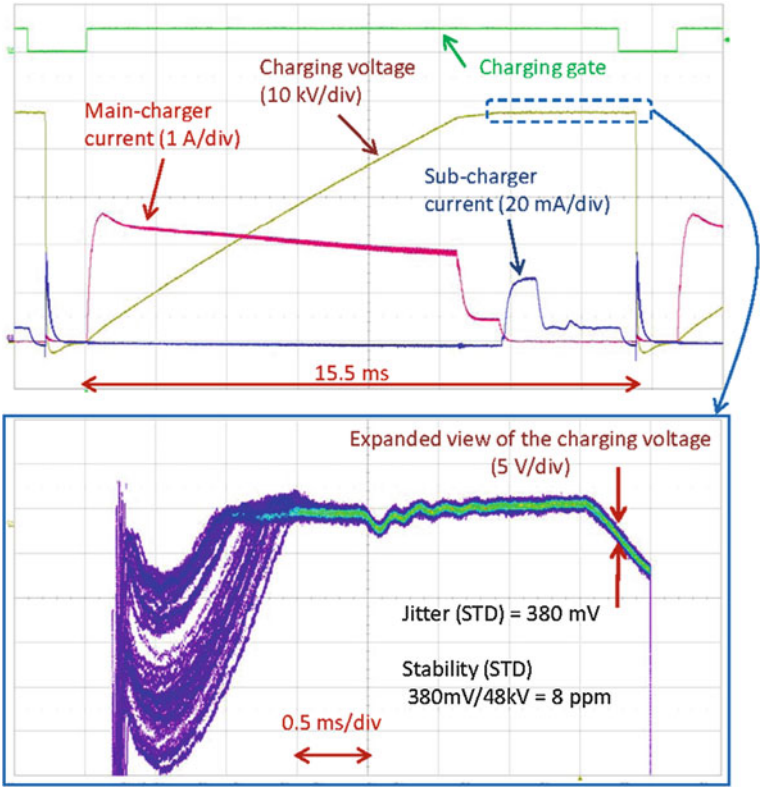

Fig. 30 Typical charging waveforms on the PFN capacitor of the modulator. The *bottom figure* shows the magnified view of the flat top part of the charging voltage, where 20 waveforms are overlaid. The voltage stability of 8 ppm in pulse-to-pulse jitter mode was achieved

high-voltage charger. If the overshoot exceeds 1%, the sub-charger will not be able to reach the target value within available time before triggering the thyratron.

To overcome this problem, the input resistance of the voltage divider was made ten times lower (100 MΩ), and as a result the settling time of the monitored voltage became shorter than 100 μs (equal to a few cycle of the main charger). In contrast, the heat generation due to higher current flow in the resistor became ten times higher (25 W at 50 kV DC). To remove heat and also regulate temperature on the dividing resistor, we developed a voltage monitor with Fluorinert immersed design as shown in Fig. 31. The monitor uses a high-precision resistor with a low-temperature coefficient of +10 ppm/°C, whose temperature is stabilized within ±10 °C by cooling water. By using this monitor, the beam energy in SACLA was stabilized within 0.03% in daily operation.

For more details on the voltage monitor, contact JAPAN FINECHEM COMPANY, INC., http://www.jfine.co.jp.

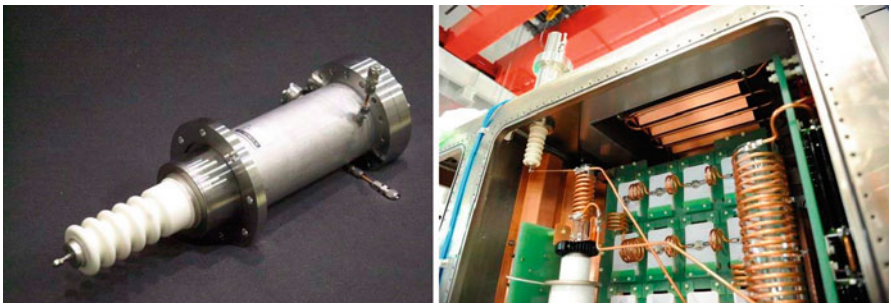

Fig. 31 High-precision fast high-voltage monitor (resistive divider). Heat generated on the high-voltage resistor is removed by cooling water through coil copper tubing. By feeding temperature-regulated water, we can maintain highly stable dividing ratio for a long period of operation. Voltage monitor was installed vertically from the top of the modulator tank, connected to the thyratron anode

Accelerating Structure

SACLA is currently running at the single-bunch mode. In the future, according to the request from X-ray experiments, it can be upgraded to multi-bunch operation (Shintake and XFEL/SPring-8 Joint Team 2010; Shintake 1992; Shintake et al. 1999). For this purpose, we employed the choke-mode cavity (Shintake 1992) in the C-band accelerator. It can damp the long-range higher-order modes (HOM) generated by a passing electron bunch inside the accelerator; thus successive bunches can be smoothly accelerated without deflecting in transverse directions. Figure 32 shows the basic concept of the choke-mode cavity. It is basically a traveling-wave accelerator of the disk-loaded structure. Microwave power travels through the series of cells, generating wave of oscillating longitudinal electric field, whose phase velocity is designed to match with particle velocity, i.e., speed of the light in the electron accelerator. In the case of the choke-mode cavity, there are additional structures: the choke and the ring-shaped silicon-carbide (SiC) ring in each cell. When a bunched beam runs through the accelerator, it generates the wakefield in its behind, which is normally reflected back from the cylindrical wall of the cavity cell and comes back to the beam axis resulting in source of the beam instability. The SiC ring acts as a microwave absorber and damps the wakefield power. The choke acts as a band-stop filter, which reflects back the C-band frequency component, and traps the traveling microwave power within the accelerating structure. The choke length is chosen to resonate at the C-band frequency with $\lambda/4$ mode. Together with TM_{010} mode in the main body of the cavity, the established mode in total becomes TM_{020}-like mode.

The choke-mode cavity was initially developed for the future e^+e^- linear collider project, where high enough beam-beam luminosity can only be achieved by the multi-bunch beam operation; thus damping of the higher-order modes was a very important issue. In the case of the X-ray FEL, if we try to boost average

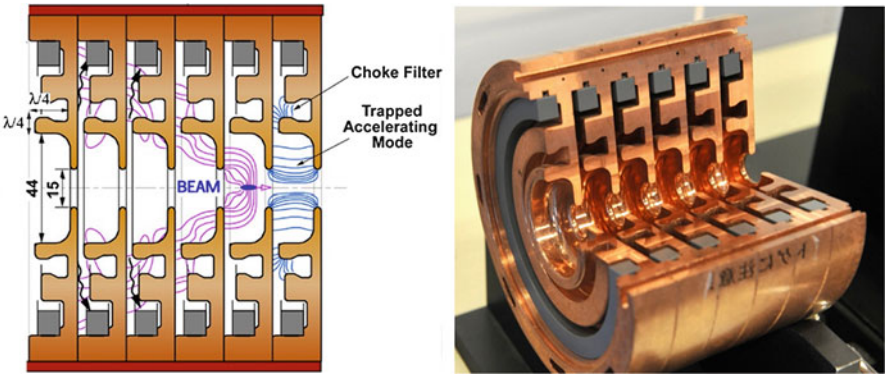

Fig. 32 The C-band choke-mode type acceleration structure

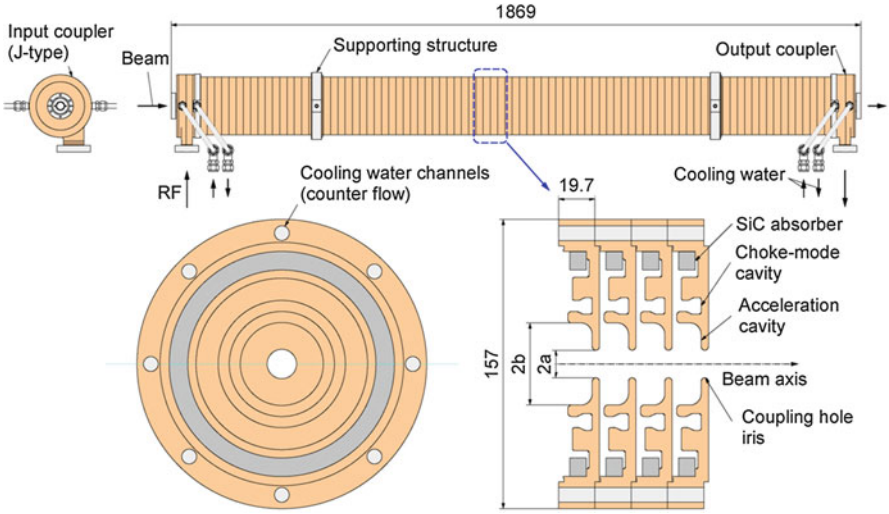

Fig. 33 The outer and cross-sectional dimensions of the accelerating structure employed at SACLA

X-ray intensity, for example, $\times$1,000 times, we will need to run multi-bunch ($\sim$100 bunches) with higher bunch charge ($\sim$1 nC), and then the higher-order mode becomes a serious issue. C-band accelerator having choke-mode cavity will easily accelerate the multi-bunch beam.

Figure 33 shows the outer dimensions and the cross-sectional view of the C-band accelerating structure employed in SACLA. Its parameters are summarized in Table 6. To fit the choke within the cell length, an rf mode of $3\pi/4$ was selected, which has 2.2 mm longer cell length than the conventional $2\pi/3$ mode. Ninety-one cavity cells, including input and output coupler cells, are assembled into a 1.8-m-long column by the metal brazing in a high-temperature vacuum furnace. In

Table 6 C-band accelerating structure

C-band frequency	5,712.00 MHz
Accelerating Structure	Quasi-CG-structure
Type of structure	Choke-mode cavity with SiC-loaded.
Structure length	1,791 mm
Number of cells	89 + 2 coupler cells
Phase advance per cell	$3\pi/4$
Cell dimension	$2a = 17.3 \sim 13.6$ mm
	$2b = 45.7 \sim 44.0$ mm
	$D = 19.68$ mm
	Disk thick ness t = 4 mm
Shunt-impedance r	49.3~60 MΩ/m
Shunt-impedance r/Q	$4.8 \sim 6.0$ kΩ/m
Quality factor	10,700 measured
Group velocity	$0.031 \sim 0.013$
Attenuation constant τ	0.53
Filling time	296 ns
Nominal energy gain	63 MeV at 35 MV/m

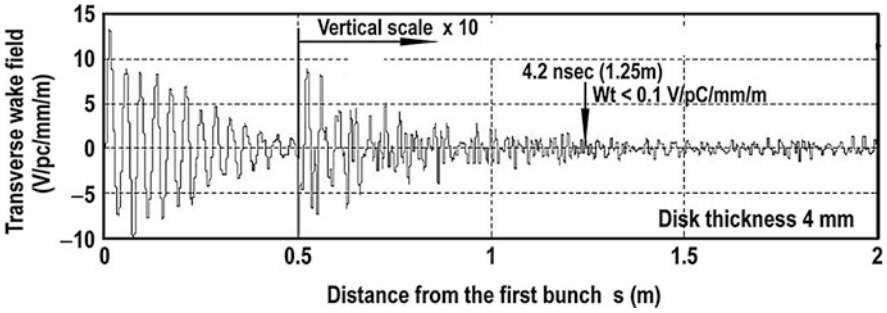

Fig. 34 The calculated transverse wakefield on the C-band accelerating structure. Thanks to the choke-mode cavity, the wakefield is damped more than 150 times at the second bunch position: 4 ns after the first bunch

order to compensate the power attenuation in the accelerating structure, the aperture diameter is linearly tapered so as to obtain a quasi-constant acceleration gradient over the structure.

Figure 34 shows the calculated transverse wakefield on the C-band accelerating structure. The dominant oscillation corresponds to TM_{110} mode at 7.5 GHz, which is strongly damped with Q-factor as low as 10. At the next bunch coming at 4.2 ns later, the wakefield becomes only 0.1 V/pC/mm/m. The wakefield was measured experimentally using e^+ and e^- beams in ASSET facility at SLAC in 1998, and the damping performance of the choke-mode cavity was confirmed (Shintake et al. 1999). As a simple estimation of the wakefield effect, assuming focusing system has an average β-function of 100 m, and alignment error of the structure refers

to the focusing system (300 μm r.m.s for 300-m-long accelerator), the transverse wakefield does not cause the beam orbit error more than one tenth of the beam spread associated with the beam emittance of 1 μrad normalized. Therefore, once the FEL beam tuning has been completed, each bunch in the multi-bunch beam will perform the same FEL performance; thus the total number of X-ray photon flux will be multiply increased. The SACLA injector uses thermionic cathode, and it is capable of generating a multi-bunch beam by simply increasing gating width of the deflection electrode right after the electron gun. Bunch separation frequency is 238 MHz (4.2 ns), and maximum number of bunch is 50, which is limited by the flat top width of input rf power to the accelerating structure.

By the way, if we simply scale down the cell dimensions from S-band to C-band, the disk thickness becomes 2.5 mm or even thinner, and then the electric field will concentrate on the aperture edge. To avoid high-voltage breakdown, we made the disk thicker, 4 mm, to lower the surface field intensity. The maximum surface field gradient was made less than 100 MV/m at nominal accelerating gradient of 35 MV/m. However, with this correction the shunt impedance was also lowered, and the choke structure also dissipates excess rf power, and as a result the shunt impedance became the same level as the S-band disk-loaded structure. However, as discussed in the previous sections, the rf power efficiency is still two times higher than the S-band case; thus we could obtain twice higher gradient in C-band accelerator with the same amount of rf power consumption.

In order to eliminate asymmetric kick associated with asymmetric power flow and transverse electric/magnetic field around the input/output couplers, we employed the J-type double-feed coupler, or sometimes called Matsumoto coupler (Suzuki et al. 1997). Thanks to the double-feed scheme, the power flow becomes up/down symmetry at the center, and the electromagnetic field becomes cylindrical symmetry around the beam axis; thus the transverse kick becomes negligibly small. It also contributes to reduce the rf-field intensity around the coupling iris.

The cavity cells were fabricated from OFHC (oxide-free high- conductivity copper, ASTM Class-1) and treated by a hot isostatic pressing (HIP) process. This treatment eliminates residual small voids in the copper material; thus it lowers the outgassing and the dark current emissions from the surface (Matsumoto 1996). The cells were initially machined on a numerical-controlled turning lathe of standard precision, including the groove of the choke and a room for the SiC ring. Then using a diamond tool on a high-precision turning lathe, the flat surface of the backside of the cell as well as the beam aperture was machined to be a mirror surface (surface roughness less than 0.1 μm) as shown in Fig. 35. Turning over the cell, from the front side, the inner surface of the cell was machined (the rf cavity part, excluding the choke). After machining, SiC rings were inserted in each cell as shown in Fig. 36, which work as microwave absorber to dump the wake filed power.

One practical problem on fabricating the choke-mode cavity is that there is no access from outside of the accelerator column to tune the resonance frequency after the metal brazing. Therefore, we needed to control the cavity dimension (especially cavity diameter $2b$) in μm range in order to tune the resonance frequency correctly,

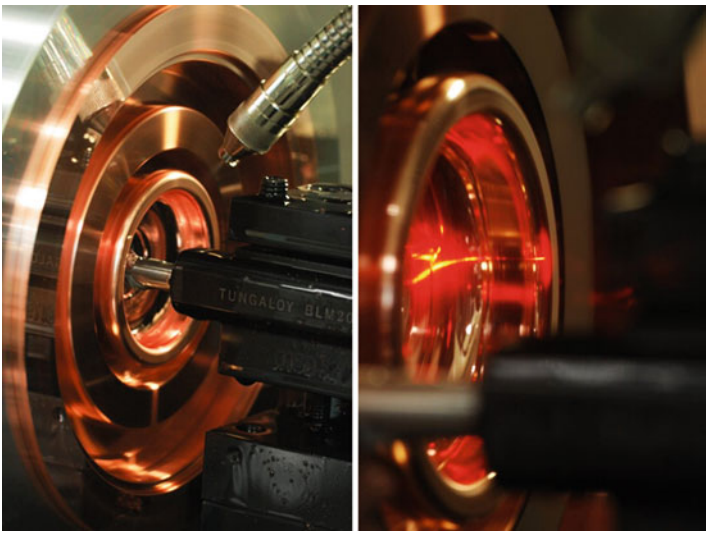

Fig. 35 The cells are fabricated from OFHC (oxygen-free high conductivity, ASTM Class-1) copper material. Final machining of the inner surface was performed by a single crystal diamond tool on a high-precision turning lathe. The axial position of the cell was precisely monitored by means of the laser distance meter

taking into account correction for a small frequency shift before/after the metal brazing. Measurement of true $2b$ dimension itself is a very difficult task, since the high-purity copper is so soft, and also small temperature change causes substantial error. To solve this problem, we performed series of measurements of resonance frequency on the cell during the final machining and applied feedback to the target dimension of $2b$. During a few steps of the cutting process, we removed the cell from the turning-lathe, quickly measured it resonance frequency by sandwiched with a flat disk at bottom with a small antenna at center and a flat cover on top with a beam hole and an antenna located behind. By detecting a resonance peak in the transmission rf signal using rf network analyzer, we measured $\pi/2$-mode frequency, from which we could find the target value of $2b$.

The high-precision turning lathe uses an air-suspended spindle, which has fairly high rigidity against lateral forces created by cutting tools, but rather loose in longitudinal direction, which causes dimension errors in machined thickness. To avoid this problem, we introduced a laser distance meter as shown in Fig. 35 and monitored the longitudinal position of the cell during the machining.

We stacked all cells in vertical on a V-shape straight, including input and output couplers at both ends as shown in Fig. 37, then laid it in horizontal. In order to confirm the electrical performance of the accelerating structure before the brazing, the rf phase was measured from the input side by moving the detuning rod step by step along 1.8-m structure. Metal brazing was performed in a vacuum furnace at temperature around 1,000 °C. To maximize production speed, two accelerator

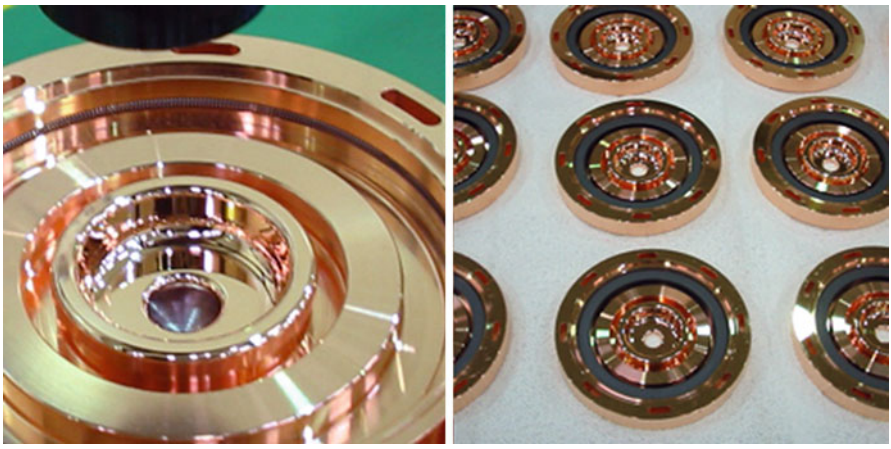

Fig. 36 The SiC ring was inserted into each cell, where a tungsten spring was used to mechanically capture the ring

Fig. 37 Eighty-nine cells and input/output couples were stacked vertically on a V-shape straight, followed by phase measurement

structures were brazed at one batch using one of the largest furnace in Japan as shown in Fig. 38 (Okihira et al. 2011).

Since 2006, the 128 acceleration structures for SACLA were manufactured with sufficient accuracy. The rf amplitude and the phase distribution were measured by the bead-pull method as shown in Figs. 39 and 40. The cell frequencies of the $3\pi/4$ mode were adjusted within ± 0.2 MHz. The integrated phase errors were kept within 2°. The quality factors of the individual cells were higher than 10,000. The straightness of the structure was about 0.1 mm, while the tolerance of the transverse offset of the structure against the single-bunch wakefield effect and the transverse kick field at the edge was 0.3 mm. Since the kick angle due to the wakefield is inversely proportional to the electron beam energy, we chose the structures having good performance, such as relatively good straightness, to install in the low-energy part of the SACLA accelerator.

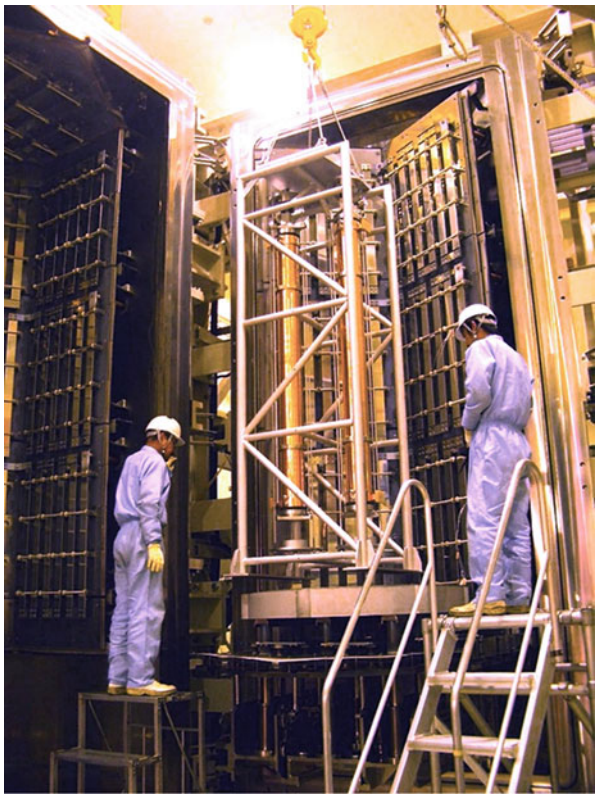

Fig. 38 Brazing two accelerator columns in a vacuum furnace

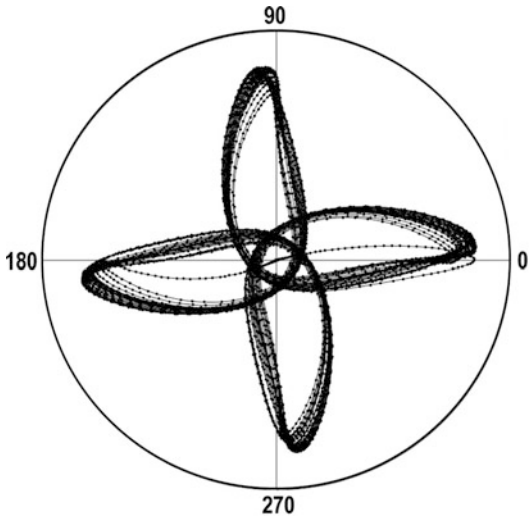

Fig. 39 Polar plot of S_{11} reflection signal from a metallic bead travels through accelerating structure after the metal brazing. Four-lobe pattern corresponds to $3\pi/4$ mode

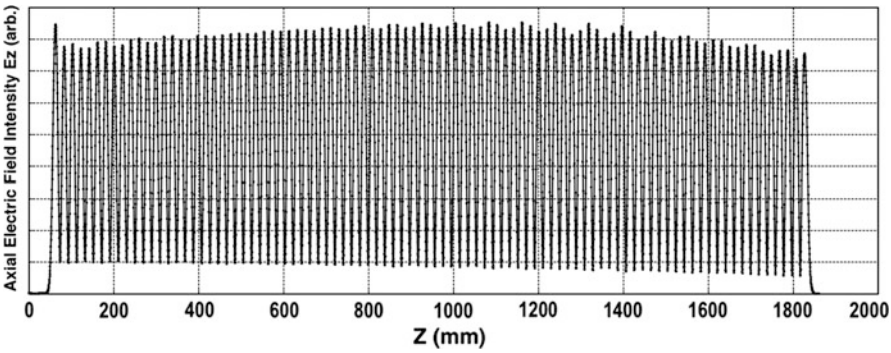

Fig. 40 The axial electric field intensity profile measured by bead-pull method after the brazing

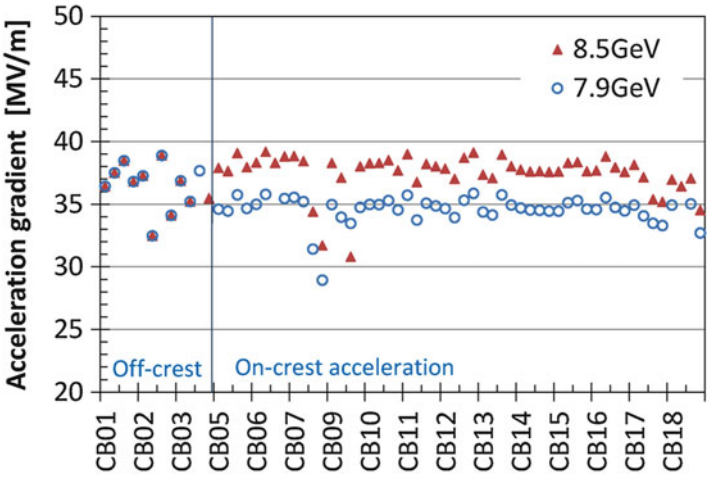

Fig. 41 Typical acceleration gradients at C-band unit in the cases of 8.5 GeV (*red triangle*) and 7.9 GeV (*blue circle*) (Inagaki et al. 2012)

Operational Experience

The rf conditioning required roughly 1,000-h operation at a designed acceleration gradient of 35 MV/m to achieve an acceptable trip rate of once per day at 10 pps repetition (Inagaki et al. 2012, 2014). The first lasing was achieved in June 2011 in this condition.

Until today, 64 C-band acceleration units have been operated for about 30,000 h, without any serious problems concerning the high-power rf components. A small problem remains on thyratron tube: randomly happening sparks, which is the main source of machine trip.

Figure 41 shows the acceleration gradient of the individual C-band acceleration units for two beam energies into undulator section. The averaged acceleration

gradients are 38 and 35 MV/m for the electron beam energies of 8.5 and 7.9 GeV, respectively. The electron beam energy was measured at several energy-dispersive points of the magnetic chicanes, and also estimated from the photon energy of the undulator radiation. The acceleration gradient of each unit was determined by measuring the energy difference with and without using the specific the acceleration unit. These measurement results agreed well with estimated value from an input rf power to the acceleration structure, within a measurement error of 10%.

A typical trip rate under an operation condition of 8 GeV, 30 pps was about once per day in each unit and once per 20 min for the whole SACLA accelerator. This trip rate was at an acceptable level for current FEL experiments. Half of the trips are roughly caused by the pre-fire of the thyratrons. About 5–10% of the interlocked trips are caused by arcing in the klystrons; the others are caused by rf breakdown in the acceleration structures. Careful study on rf breakdown issues have been reported (Inagaki et al. 2014).

The pulse-to-pulse stabilities of the PFN voltage, klystron voltage, rf amplitude, and phase of the klystron output were measured and are summarized in Table 7. Thanks to precise regulation of the PFN voltage, the rf amplitude and phase were within tolerances of 0.01% and 0.2°, required by the X-ray FEL operation, although many of these values were limited by the resolutions of the measurement instruments. The drift of the rf phase is corrected by the feedback control of the LLRF system. In addition, drifts of the electron beam energy and trajectory due to the rf power variation are compensated by several feedback loops. The stability of the final electron beam energy is consequently 0.02% in standard deviation in the pulse-to-pulse fluctuation and 0.03% in the peak-to-peak in the long-term drift. These values are smaller than the energy spread of the electron beam of 0.1% and a spectral bandwidth of the X-ray laser of 0.3% in FWHM. Therefore, the acceleration field amplitude of the C-band accelerator has sufficient stability to generate a stable laser for user experiments.

Although the acceleration structure has the choke structure for wakefield absorption, multi-bunched beam operation has not yet been tested. It will be utilized for a future upgrade of SACLA.

Table 7 Typical values of pulse-to-pulse stabilities of the rf amplitude and the phase at the klystron output, klystron voltage and current, and charging voltage in standard deviations. The values in the bracket are the measurement error, estimated by the fluctuation of the ground potential

Modulator charging voltage	0.0007% (0.0007%)
Klystron cathode voltage	0.0024% (0.0016%)
Klystron beam current	0.0025% (0.0018%)
RF amplitude of klystron output	0.0092% (0.0075%)
RF phase of klystron output	0.03°

Summary

Since 2011, 8-GeV C-band accelerator is routinely operating at SACLA X-ray laser in SPring-8 Japan with accelerating gradient higher than the design value of 35 MV/m.

C-band accelerator is so reliable, which will be suitable for full energy injector for light sources with top-up operation; 3-GeV beam is available within 100-m-long tunnel. European S-band is 2,998.5 MHz, which is 142.5 MHz higher than US S-band (2,856 MHz). Combination of 5,712 MHz C-band (= 2,856 MHz × 2) with European S-band is also possible with proper design of frequency mixing and injector timing control.

If an application does not require a multi-bunch beam, a simple disk-loaded structure can be used instead of the choke-mode cavity or other HOM damping structures, where one can fully gain benefit from the high shunt-impedance of C-band frequency, i.e., higher gradient with lower power consumption and higher machine repetition rate. C-band accelerator will open new science and industry applications in the future.

Acknowledgments The author would like to thank all contributors on C-band R&D and SACLA construction. The author wishes to acknowledge specially Dr. Hiroshi Matsumoto and Dr. Masakazu Yoshioka for their long periods of supports and encouragements. Finally, the author would like to thank Dr. Takahiro Inagaki for his excellent contribution on C-band system development by designing details, careful quality test, and patiently debugging the whole system; without his effort we could not achieve this result.

The author would like to thank the industry people who contributed to C-band R&D and SACLA construction with careful and patient work, especially Dr. Sadao Miura and Dr. Atsushi Miura for their excellent contributions on C-band high power waveguide and accelerator development, and Dr. Yoshihisa Ohkubo for his extensive work on 50 MW C-band klystron development. Finally, the author would like to thank Prof. Hitoshi Baba for his various contributions and long period of encouragement to us.

References

T. Bizen, Development of vacuum components for XFEL/SPring-8, in *Proceedings of EPAC08, 11th European Particle Accelerator Conference*, Genoa, 23–27 June 2008 (2008)

Z.D. Farkas et al., SLED: a method of doubling SLAC's energy, SLAC-PUB-1453, June 1974

T. Inagaki et al., High gradient operation of 8 GeC C-band accelerator in SACLA, in *Proceedings of LINAC2012*, Tel-Aviv (2012)

T. Inagaki, C. Kondo, H. Maesaka, T. Ohshima, Y. Otake, T. Sakurai, K. Shirasawa, T. Shintake, High-gradient C-band linac for a compact x-ray free-electron laser facility. PRST-AB Phys. Rev. Spec. Top. Accel. Beams **17**, 080702 (2014)

T. Ishikawa et al., A compact X-ray free-electron laser emitting in the sub-angstrom region. Nat. Photon. **6**, 540–544 (2012). 2012.141

A. Jensen et al., 25 year performance review of the SLAC 5045 S-band klystron, in *Proceedings of IPAC2011*, San Sebastian (2011)

C. Kondo, T. Inagaki, K. Shiarasawa, T. Sakurai, T. Shintake, Cooling system design of compact klystron modulator power supply in the XFEL Project at SPring-8, in *Proceedings of the LINAC08*, Victoria, 2008

LC Group, JLC-I, KEK Report 92-16, Dec 1992, A/H/M (1992)
H. Maesaka et al., Development of the optical timing and RF distribution system for XFEL/SPring-8, in *Proceedings of FEL'08*, Gyeongju (2008), p. 352
H. Matsumoto, Dark currents, in *Proceedings in LINAC'96, XVIII International Linac Conference*, Geneva, 26–30 Aug 1996 (1996)
H. Matsumoto et al., R&D of the C-band klystron modulator, in *Presented at: 2nd Modulator-Klystron Workshop for Future Linear Colliders*, Stanford, Oct 1995 [SLAC 481], pp. 138–147 (1995)
H. Matsumoto, T. Shintake, N. Akasaka, Development of C-band (5712 MHz) high power waveguide components, in *Proceeding PAC'97, Particle Accelerator Conference*, Vancouver, 12–16 May 1997 (1997)
R.B. Neal, The Stanford two-mile linear accelerator, SLAC -PUB-233. Stanford Linear Accelerator Center, Stanford University, Stanford (1966)
J.S. Oh et al., Efficiency issue in C-band klystron-modulator system for linear collider, in *Proceeding PAC,97, 1997 Particle Accelerator Conference*, Vancouver, 12–16 May 1997 (1997)
J.S. Oh et al., Development of a smart modulator and efficiency evaluation of 500-GeV $e^+ e^-$ C-band linear collider, in *Proceedings of 20th International Linear Accelerator Conference (LINAC'2000)*, Monterey (2000)
Y. Ohkubo et al., The C-band 50MW klystron using traveling-wave output structure, in *Proceedings of 19th International Linear Accelerator Conference (LINAC'98)*, Chicago (1998)
K. Okihira et al., Mass production report of C-band choke mode accelerating structure and rf pulse compressor, in *IPAC2011*, San Sebastian (2011)
Y. Otake et al., Beam monitor system for an x-ray free electron laser and compact laser. Phys. Rev. ST Accel. Beams **16**, 042802 (2013)
SCSS X-FEL R&D Group, SCSS XFEL Conceptual Design Report, edited by T. Shintake and T. Tanaka, RIKEN/SPring-8, Japan (2004)
T. Shintake, The choke mode cavity. Jpn. J. Appl. Phys. **31**, L1567–L1570 (1992)
T. Shintake, Klystron simulation and design using the Field Charge Interaction (FCI) code. Nucl. Instrum. Methods Phys. Res. A **363**, 83–89 (1995)
T. Shintake, Recent status of FCI: PIC simulation of coupled-cavity structure, in *LINAC96, XVIII International Linear Accelerator Conference*, Geneva, 26–30 Aug 1996 (1996)
T. Shintake et al., C-band linac RF-system for $e^+ e^-$ linear collider, in *Proceedings of 16th Biennial Particle Accelerator Conference: PAC'95*, Dallas (1995)
T. Shintake, N. Akasaka, H. Matsumoto, Development of C-band 50 MW Pulse Klystron for $e^+ e^-$ Linear Collider, in *Proceedings of the International Particle Accelerator Conference (PAC97)*, Vancouver, 12–16 May 1997 (1997a)
T. Shintake, N. Akasaka, H. Matsumoto, Development of C-band RF pulse compression system for $e^+ e^-$ linear collider, in *PAC'97, Particle Accelerator Conference*, Vancouver, 12–16 May 1997 (1997b)
T. Shintake et al., Results from hardware R&D on C-band RF-system for $e^+ e^-$ linear collider, in *proceedings of XIX International Linac Conference LINAC98*, Chicago, Aug 1998
T. Shintake et al., The first wakefield test on the C-band choke-mode accelerating structure, in *Proceedings of PAC'99*, New York (1999)
T. Shintake et al., SPring-8 compact SASE source (SCSS), in *SPIE's 46th Annual Meeting, The International Symposium on Optical Science and Technology*, San Diego, 29 July–3 Aug 2001
T. Shintake et al., Status of SPring-8 compact SASE source FEL project, NIM A21188. Nucl. Instrum. Methods Phys. Res. A **507**, 382–397 (2003)
T. Shintake et al., A compact free-electron laser for generating coherent radiation in the extreme ultraviolet region. Nat. Photon. **2**, 555–559 (2008)
T. Shintake et al., Stable operation of a self-amplified spontaneous-emission free-electron laser in the extremely ultraviolet region. Phys. Rev. ST Accel. Beams **12**, 070701 (2009)
T. Shintake, Compact klystron modulator for XFEL/SPring-8, in *IPAC'10*, Kyoto, p. 3287 (2010)
T. Shintake, XFEL/SPring-8 Joint Team, Status report on Japanese XFEL construction project at SPring-8, in *Proceedings of IPAC'10*, Kyoto (2010)

C. Suzuki et al., Input coupler design for C-band accelerating structure, in *Proceeding 17th IEEE Particle Accelerator Conference (PAC 97)*, Vancouver, 12–16 May 1997 (1997)
H. Tanaka et al., Low Emittance Injector at SCSS, Prod. FEL2006, Aug 2006, BESSY, Berlin (2006)
R. Tanaka et al., First operation of the SACLA control system in Spring-8, in *Proceedings of IPAC2011*, San Sebastián (2011)
K. Togawa et al., CeB6 electron gun for low-emittance injector. Phys. Rev. ST Accel. Beams **10**, 020703 (2007)